

University of Dundee

## Activation of NF- $\kappa$ B and p300/CBP potentiates cancer chemoimmunotherapy through induction of MHC-I antigen presentation

Zhou, Yixuan; Bastian, Ingmar Niels; Long, Mark D.; Dow, Michelle; Li, Weihua; Ngu, Rachael  
Katie

*Published in:*  
Proceedings of the National Academy of Sciences

*DOI:*  
[10.1073/pnas.2025840118](https://doi.org/10.1073/pnas.2025840118)

*Publication date:*  
2021

*Document Version*  
Peer reviewed version

[Link to publication in Discovery Research Portal](#)

### *Citation for published version (APA):*

Zhou, Y., Bastian, I. N., Long, M. D., Dow, M., Li, W., Ngu, R. K., Antonucci, L., Huang, J. Y., Phung, Q. T., Zhao, X., Banerjee, S., Lin, X.-J., Wang, H., Dang, B., Choi, S., Karin, D., Su, H., Ellisman, M. H., Jamieson, C., ... Shalapour, S. (2021). Activation of NF- $\kappa$ B and p300/CBP potentiates cancer chemoimmunotherapy through induction of MHC-I antigen presentation. *Proceedings of the National Academy of Sciences*, 118(8), [e2025840118]. <https://doi.org/10.1073/pnas.2025840118>

### **General rights**

Copyright and moral rights for the publications made accessible in Discovery Research Portal are retained by the authors and/or other copyright owners and it is a condition of accessing publications that users recognise and abide by the legal requirements associated with these rights.

- Users may download and print one copy of any publication from Discovery Research Portal for the purpose of private study or research.
- You may not further distribute the material or use it for any profit-making activity or commercial gain.
- You may freely distribute the URL identifying the publication in the public portal.

### **Take down policy**

If you believe that this document breaches copyright please contact us providing details, and we will remove access to the work immediately and investigate your claim.



**Activation of NF- $\kappa$ B and p300/CBP potentiates cancer chemoimmunotherapy through induction of MHC-I antigen presentation**

Yixuan Zhou<sup>a,1</sup>, Ingmar Niels Bastian<sup>a,1</sup>, Mark D Long<sup>b,1</sup>, Michelle Dow<sup>c,1</sup>, Weihua Li<sup>a,d,1</sup>, Tao Liu<sup>b</sup>, Rachael Katie Ngu<sup>a</sup>, Laura Antonucci<sup>a,d</sup>, Jian Yu Huang<sup>a,d</sup>, Qui T Phung<sup>e</sup>, Xi-he Zhao<sup>a,d,f</sup>, Sourav Banerjee<sup>a,g</sup>, Xue-Jia Lin<sup>a,d,h</sup>, Hongxia Wang<sup>i</sup>, Brian Dang<sup>a,d</sup>, Sylvia Choi<sup>a,d</sup>, Daniel Karin<sup>a</sup>, Hua Su<sup>a,d</sup>, Mark H. Ellisman<sup>j</sup>, Christina Jamieson<sup>k</sup>, Marcus Bosenberg<sup>l</sup>, Zhang Cheng<sup>m</sup>, Johannes Haybaeck<sup>n,o</sup>, Lukas Kenner<sup>p,q</sup>, Kathleen M. Fisch<sup>r</sup>, Richard Bourgon<sup>e</sup>, Genevive Hernandez<sup>e</sup>, Jennie R. Lill<sup>e</sup>, Song Liu<sup>b</sup>, Hannah Carter<sup>c</sup>, Ira Mellman<sup>e</sup>, Michael Karin<sup>a,b,\*</sup>, Shabnam Shalpour<sup>a,s,\*</sup>,<sup>2</sup>

<sup>a</sup> Department of Pharmacology, School of Medicine, University of California San Diego, CA 92093, USA

<sup>b</sup> Department of Biostatistics and Bioinformatics, Roswell Park Comprehensive Cancer Center, Buffalo, NY 14263, USA

<sup>c</sup> Division of Medical Genetics, Health Sciences, Department of Biomedical Informatics, Department of Medicine, University of California, San Diego, La Jolla, CA 92093, USA

<sup>d</sup> Laboratory of Gene Regulation and Signal Transduction, Department of Pharmacology, School of Medicine, University of California San Diego, 9500 Gilman Drive, La Jolla, CA 92093, USA

<sup>e</sup> Genentech, Inc., 1 DNA Way, South San Francisco, CA 94080, USA

<sup>f</sup> China Medical University Shengjing Hospital Oncology Department, No. 36 Sanhao Street, Heping District, Shenyang City, Liaoning Province, 110004, China

<sup>g</sup> Department of Cellular Medicine, Jacqui Wood Cancer Centre, University of Dundee, James Arrott Drive, Dundee DD1 9SY, United Kingdom.

<sup>h</sup> Biomedical Translational Research Institute and the First Affiliated Hospital, Jinan University, 601 West Huangpu Road, Guangzhou, Guangdong, China, 510632

<sup>i</sup> National Center of Biomedical Analysis, 27 Taiping Road Beijing China 100850

<sup>j</sup> National Center for Microscopy and Imaging Research, Center for Research in Biological Systems, University of California, San Diego, La Jolla, CA, 92093, USA.

<sup>k</sup> Department of Urology, Moores Cancer Center, University of California San Diego, CA 92093, USA

<sup>l</sup> Yale School of Medicine, 15 York Street, St LMP 5031, New Haven, CT, 06510, USA

<sup>m</sup> Center for Epigenomics, Department of Cellular and Molecular Medicine, University of California, San Diego, School of Medicine, 9500 Gilman Dr, La Jolla, CA 92093, USA

<sup>n</sup> Institute of Pathology, Medical University of Graz, Graz A-8036, Austria

<sup>o</sup> Department of Pathology, Neuropathology and Molecular Pathology, Medical University of Innsbruck, Innsbruck A-6020, Austria

<sup>p</sup> Department of Pathology, Christian Doppler Laboratory, Medical University of Vienna, 1090 Vienna, Austria

<sup>q</sup> Unit of Pathology of Laboratory Animals (UPLA), University of Veterinary Medicine Vienna, 1210 Vienna, Austria

<sup>r</sup> Center for Computational Biology & Bioinformatics, Department of Medicine, University of California, San Diego, La Jolla, CA 92093, USA

<sup>s</sup> Department of Cancer Biology, University of Texas MD Anderson Cancer Center, Houston, TX 77054, USA

\***Correspondence:** Michael Karin, Shabnam Shalapour.

**Email:** karinoffice@ucsd.edu, sshalapour@mdanderson.org

<sup>1</sup>Y.Z., I.N.B., M.D.L., M.D. and W.L. contributed equally to this work.

<sup>2</sup>Lead Contact

**Competing Interest Statement:** I. Mellman, JR. Lill, R. Bourgon, Q. T Phung and G. Hernandez are employees of Genentech. All other authors declare no competing financial interests.

**Classification:** **BIOLOGICAL SCIENCES**, Immunology and Inflammation; Medical Sciences

**Keywords:** histone acetylation, NF- $\kappa$ B, MHCII, antigen presentation, immune checkpoint inhibitors, Chemotherapy

**This PDF file includes:**

Main Text: 4639

Figure 1: medium (11.3cm x 10.3cm)

Figure 2: large (16.6cm x 21.2cm)

Figure 3: large (15.4cm x 11.7cm)

Figure 4: medium (9.6cm x 11.0cm)

Figure 5: medium (11.4 cm x 9.4cm)

Figure 6: medium (10.2cm x 11.0cm)

Figure 7: large (16.4cm x 15.3cm)

Figure 8: small (9.0cm x 6.4cm)

## **Abstract**

Many cancers evade immune rejection by suppressing MHC-I antigen processing and presentation (AgPP). Such cancers do not respond to immune checkpoint inhibitor therapies (ICIT) such as PD-1/PD-L1 [PD-(L)1] blockade. Certain chemotherapeutic drugs augment tumor control by PD-(L)1 inhibitors through potentiation of T cell priming but whether and how chemotherapy enhances MHC-I dependent cancer cell recognition by cytotoxic T cells (CTL) is not entirely clear. We now show that the lysine acetyl transferases p300/CBP control MHC-I AgPPM expression and neoantigen amounts in human cancers. Moreover, we found that two distinct DNA damaging drugs, the platinoid oxaliplatin and the topoisomerase inhibitor mitoxantrone, strongly upregulate MHC-I AgPP in a manner dependent on activation of NF- $\kappa$ B, p300/CBP and other transcription factors, but independently of autocrine IFN $\gamma$  signaling. Accordingly, NF- $\kappa$ B and p300 ablations prevent chemotherapy-induced MHC-I AgPP and abrogate rejection of low MHC-I expressing tumors by re-invigorated CD8<sup>+</sup> CTL. Drugs like oxaliplatin and mitoxantrone may be used to overcome resistance to PD-(L)1 inhibitors in tumors that had “epigenetically downregulated”, but had not permanently lost MHC-I AgPP activity.

## **Significance Statement**

T cells recognize their targets via their T cell receptors (TCR), which in the case of CD8<sup>+</sup> T cells bind to MHC-I:antigen complexes on the surface of target cells. Many cancer cells evade immune recognition and killing by downregulating MHC-I AgPPM. Here, we show how the histone acetyl transferases P300/CBP together with NF- $\kappa$ B epigenetically regulate expression of MHC-I molecules, immunoproteasome subunits and peptide transporter to enable proper MHC-I antigen presentation. Notably, this pathway is frequently disrupted in human cancers. We now show that certain chemotherapeutics can augment MHC-I antigen presentation via NF- $\kappa$ B and p300/CBP activation thereby enhancing cancer cell recognition and killing by effector CD8<sup>+</sup> CTLs.

## Main Text

### Introduction

Immune checkpoint inhibitor therapy (ICIT) had transformed cancer treatment (1–4), but even in ICIT-responsive metastatic melanoma and non-small cell lung cancer (NSCLC), response rates rarely exceed 40% (5). Other malignances, including prostate cancer (PCa) and pancreatic ductal adenocarcinoma (PDAC), are ICIT refractory (6–9). For a given neoplasm to respond to immune checkpoint inhibition, in particular PD-(L)1 blockade, it needs to be populated by CTL that recognize tumor antigens (4). However, even CTL populated tumors can evade immune elimination either through activation of immunosuppressive mechanisms that induce CD8<sup>+</sup> T cell suppression or restrain their entry into tumors (10), down-regulation of MHC-I AgPP (11, 12) or antigen editing and loss (13). Various strategies have been used to enhance ICIT responsiveness, including induction of immunogenic cell death (ICD) by radiotherapy and chemotherapy (14). By enhancing the release of damage associated molecular patterns (DAMP) and other molecules, ICD stimulates tumor antigen uptake by antigen-presenting cells (APC) that prime T cells against tumor antigens, as demonstrated by vaccination experiments (15). Primed T cells may accumulate in the tumor and lead to immune rejection as long as they can recognize and kill their targets (16). Such strategies are ineffective in cancers with low MHC-I or HLA-A/B/C expression (11, 16–19).

PCa is a typical ICIT-refractory cancer, presumably due to low expression of HLA-A/B/C molecules that together with  $\beta$ 2 macroglobulin form MHC-I heterodimers, which present tumor antigens to CD8<sup>+</sup> CTL (20, 21). Using mouse models of PCa we found that the platin-based DNA-crosslinker oxaliplatin (Oxali) potentiates immune rejection of autochthonous or engrafted tumors after genetic or pharmacological depletion of PD-L1-expressing immunosuppressive IgA<sup>+</sup> plasmocytes, which cause CTL exhaustion (22). Low dose Oxali also enhances mouse PCa regression in response to anti-PD-L1 treatment (22). Similar results were obtained with low dose Oxali or photodynamic therapy in other cancer models (23, 24) but the underlying mechanisms have not been explored. As Oxali is known to induce ICD and T cell priming, we investigated whether its ability to potentiate the immune rejection of IgA<sup>+</sup> plasmocyte-depleted or anti-PD-L1 treated low MHC-I prostate tumors also entails effects on the recognition and killing step of the cancer immunity cycle, which depends on CTL-MHC-I interactions (16, 25). Here we show that Oxali and the structurally unrelated topoisomerase II inhibitor mitoxantrone (Mito) transcriptionally upregulate expression of MHC-I molecules and their cognate antigen presentation and processing machinery (AgPPM). This response, which takes place in human and mouse cancers, depends on activation of NF- $\kappa$ B and nuclear translocation of the closely related histone (and lysine) acetyl transferases p300 and CREB binding protein (CBP). Whereas p300 ablation abrogated MHC-I AgPP induction and the synergy between low dose Oxali and PD-(L)1 blockade, it had no effect on induction of anti-tumor immunity by Oxali-killed PCa cells used as an immunogen.

### Results

#### Oxaliplatin and mitoxantrone induce MHC-I AgPPM genes

To determine the effect of Oxali and related drugs on gene expression in PCa cell lines used in our previous study (22), Myc-CaP cells were treated with different drugs at doses that induce no more than 10 % cell death, and vital cells (SI Appendix, Fig. S1A and S1B) were analyzed by whole genome RNA sequencing (RNAseq) and ATAC-seq (Assay for Transposase-Accessible Chromatin) (26). Since CTL re-invigoration by anti-PD-L1 induces IFN $\gamma$  production (27, 28), we also examined the effect of IFN $\gamma$  alone or together with chemotherapy. Low-dose chemotherapy, in particular Oxali, induced marked changes in gene expression and chromatin accessibility depicted as Differentially Expressed Genes (DEG) and Differentially Accessible DNA Regions (DAR) (Fig. 1A and SI Appendix, Fig. S1C-S1F). The platinoid-induced changes were usually augmented by IFN $\gamma$ , although the effects of Oxali were broader than that of

IFN $\gamma$ , which mainly enhanced gene expression magnitude rather than breadth. Some of the Oxali or IFN $\gamma$  inducible gene sets were common to both agents (Fig. 1A). Pathway enrichment analysis (Fig. 1B) identified the most significantly enriched pathways, activated by Oxali (red, e.g. Epithelial-mesenchymal transition, TP53), IFN $\gamma$  (blue, e.g. Myc) or Oxali + IFN $\gamma$  together (purple, e.g. IFN type I and II, AgPPM). Notably, while either Oxali or IFN $\gamma$  significantly enriched genes involved in MHC-I AgPP and IFN $\gamma$  signaling, these effects were strongly enhanced when Oxali and IFN $\gamma$  were combined (Fig. 1B and [SI Appendix, Fig. S2A-S2C](#)). However, Oxali did not induce IFN $\gamma$  expression, indicating that its ability to induce MHC-I AgPPM components was not due to autocrine IFN $\gamma$  signaling.

Pathway enrichment analysis of DEGs that were responsive to Oxali plus IFN $\gamma$  revealed strong induction of genes related to type I and II IFN signaling and MHC-I AgPPM components, involved in protein folding, MHC-I complex assembly and peptide loading, as well as genes involved in the ER-phagosome pathway and anti-viral responses (Fig. 1C and [SI Appendix, Fig. S2D](#)). Most of these genes were also induced by Oxali alone. To understand how these genes were induced we examined the ATAC-seq patterns of a gene cluster on mouse chromosome 17 harboring the *Psmb9*, *Tap1*, *Psmb8*, and *Tap2* genes, coding for immunoproteasome components and peptide transporters ([SI Appendix, Fig. S1E-S1F and S3A](#)). Low dose Oxali, and to a lesser extent Cisplatin (Cispl), increased transcription factor (TF) accessibility at several sites within this locus ([SI Appendix, Fig. S3A](#)). Surprisingly, IFN $\gamma$  alone had little effect, if any, on chromatin structure ([SI Appendix, Fig. S1F](#)). Q-RT-PCR analysis further confirmed induction of AgPPM genes by Oxali and Cispl and to a lesser extent by Mito, alone or together with IFN $\gamma$  ([SI Appendix, Fig. S3B-S3D](#)). A similar response pattern was displayed by the *Nlrc5* gene coding for NLRC5/CITA, the master activator of the MHC-I AgPPM (Fig. 2A). ATAC-seq revealed increased *Nlrc5* chromatin accessibility after low dose Oxali or Cispl, but hardly any change after IFN $\gamma$  treatment (Fig. 2B). Mito, Cispl and Oxali, but not IFN $\gamma$ , induced *Ifngr2* mRNA, but had little effect on chromatin accessibility of its gene (Fig. 2C-2D). Of note, the chromosome 17 region opened up by Oxali contains binding motifs recognized by BORIS and CTCF ([SI Appendix, Fig. S3A](#)), general TF responsible for chromatin opening (29). Low dose Oxali also increased  $\beta$ 2 microglobulin ( $\beta$ 2M) and all tested chemotherapeutics induced surface and mRNA expression of H-2Kq, the predominant MHC-I molecule in Myc-CaP cells (Fig. 2E-2F and [SI Appendix, Fig. S3D](#)). Low-dose Oxali increased immunoproteasome activity measured with an LMP7/PSMB8-specific substrate, Ac-ANW-AMC, an effect that was potentiated by IFN $\gamma$  (Fig. 2G).

### Putative transcriptional regulators of MHC-I AgPPM induction

We searched for signaling pathways and TF mediating MHC-I AgPPM and IFN $\gamma$ R2 induction by low dose Oxali. RNA-seq and pathway enrichment analyses suggested involvement of IRF, STAT, NF- $\kappa$ B, MYC family members and androgen receptor (AR) (Fig. 2H-2K, and [SI Appendix, Fig. S3E-S3F](#)). Whereas the IRF, STAT and NF- $\kappa$ B pathways were upregulated by Oxali and potentiated by IFN $\gamma$ , the MYC and to a lesser extent the AR pathway, both of which participate in PCa tumorigenesis (30–32), were downregulated after Oxali + IFN $\gamma$  treatment. Amongst IRF family members, IRF1, 7 and 9 were stimulated by Oxali and IFN $\gamma$ , IRF2 was induced by Oxali and IRF8 mainly responded to IFN $\gamma$  ([SI Appendix, Fig. S3F](#)). Similarly, STAT1 and 2 were stimulated by Oxali, whereas IFN $\gamma$  induced STAT1 and 3. JUN, ATF3, UBA7, CREB3, NFE2L1 and SOCS1 were induced by low-dose Oxali, along with NF- $\kappa$ B1 (p105) and NF- $\kappa$ B2 (p100) ([SI Appendix, Fig. S3F](#)). ATAC-seq confirmed that Oxali, but not IFN $\gamma$ , enhanced chromatin accessibility of the *Nfkb1* locus (Fig. 2H).

We employed two additional analytic approaches to identify master TF mediating treatment-induced expression changes [LISA (33)] and TF binding enrichment within regions of differential chromatin accessibility [GIGGLE (34)]. These analyses predicted the master regulators (MRs) most likely to influence the DEGs (Fig. 2I) and DARs (Fig. 2J) by leveraging the complete set of TF binding datasets



available from the CistromeDB collection. The results further highlighted treatment-related directional TF associations (up/downregulated DEGs, open/closed DARs); Oxali: ESR1, NR3C1 and JUN; IFN $\gamma$ : MYC, STAT1, ATF4 and FOS; Oxali + IFN $\gamma$ : STAT1, YAP1, ESR1, IRF1, RELA and IRF8 (Fig. 2I-2J). DEG and DAR integration revealed 200 common TF, including IRFs and STATs (Fig. 2K). Notably, Oxali treatment elicited marked changes in histone methylation- and acetylation-related gene signatures (Fig. 2L) in agreement with the ATAC-seq data (SI Appendix, Fig. S1E-S1F). Subset analyses focusing on histone modifying factors implicated the involvement of the histone acetyltransferases (HATs) p300 and CBP and several histone deacetylases (HDACs) (SI Appendix, Fig. S4A).

To confirm induction and/or activation of some of the above TF, PCa (Myc-CaP, TRAMP-C2/TRC2) and colon cancer (MC38) cell lines were treated as above with or without IFN $\gamma$ . Protein immunoblotting (IB) and flow cytometric analyses confirmed induction of ER stress (P-eIF2 $\alpha$ , CHOP) and DNA damage (p-p53,  $\gamma$ H2AX, p-ATM) markers, IRFs (IRF1, p-IRF3, IRF7), STATs (P-STAT1 and STAT1), CREB1, JUNB, type I IFN inducing proteins (cGAS, STING), PSMB9, and NF- $\kappa$ B signaling components (I $\kappa$ B $\alpha$ , RELA/p65, P-p65) (SI Appendix, Fig. S4B-S4G).

### **Chemotherapy stimulates HAT nuclear localization and activity**

Chromatin structure opening, as revealed by ATAC-seq analysis, depends on histone acetylation (35). Importantly, Oxali treatment of Myc-CaP cells, increased HAT enzymatic activity within 3 h and its effect was comparable to that of an HDAC inhibitor (HDACi) (Fig. 3A-3B). Oxali and Mito also increased total p300, acetylated CBP/p300 and K310-acetylated RELA/p65 nuclear amounts (Fig. 3C). IFN $\gamma$  also increased nuclear p300, but its effect was considerably weaker than that of Oxali (Fig. 3C-3D). Both Oxali and HDACi induced p300 nuclear translocation in murine PCa cells (Fig. 3D) and human PCa organoids (SI Appendix, Fig. S5A). ChIP experiments showed that Oxali induced p300 and RELA/p65 recruitment to the *Nlrc5* and *Ifngr2* promoters and p300 recruitment to the *Tap1*, *Psmb8/9* promoters (Fig. 3E-3F). These promoter regions also exhibited increased H3K14 and K27 acetylation after Oxali treatment (Fig. 3G). Oxali-induced H3K14 acetylation at nuclear foci, similar to those revealed by p300 antibody staining, was also observed by IF analysis (SI Appendix, Fig. S5B). Increased RELA/p65 K310 acetylation, which was attenuated after treatment by p300/CBP inhibitors, was confirmed by IB and IF analyses (SI Appendix, Fig. S5C-S5D). Using HA- or Myc-tagged *p300* and Flag-tagged *Stat1* expression vectors followed by immunoprecipitation (IP), we confirmed binding of p300 to endogenous RELA/p65 and transfected STAT1 (SI Appendix, Fig. S5E), an interaction that stimulates p300 acetyltransferase activity (36). To investigate the basis for p300 nuclear translocation, we examined induction of HLA-B-associated transcript 3 gene product, BAT3, which controls intracellular p300 distribution (37). IF analysis confirmed Oxali-induced nuclear translocation of both p300 and BAT3 (SI Appendix, Fig. S5F).

### **p300 and CBP control MHC-I AgPPM expression and neoantigen amounts**

We generated cell lines deficient in p300 or CBP (Fig. 4A and SI Appendix, Fig. S6B). p300 $^{\Delta}$ -Myc-CaP cells expressed CBP and upregulated its expression upon Oxali treatment, and CBP $^{\Delta}$ -Myc-CaP cells behaved similarly. Notably, p300 $^{\Delta}$ -Myc-CaP cell viability did not differ from that of parental cells and neither p300 nor CBP ablation reduced total or Oxali-induced total RELA/p65 protein or *Nfkb1a* mRNA (Fig. 4A and SI Appendix, Fig. S6A-S6C). However, *Tap1*, *Psmb9*, *Nlrc5*, *Ifngr2* and *Ifna* mRNA inductions were attenuated by both p300 or CBP ablations, whereas *Irf1* and *Erap1* mRNA inductions were only reduced in p300 $^{\Delta}$ -Myc-CaP cells (Fig. 4B-4F and SI Appendix, Fig. S6D-S6E). Both the p300 and CBP deficiencies attenuated induction of *Sec22b* mRNA (Fig. 4G), coding for a vesicle-trafficking protein that regulates phagosomal maturation and antigen crosspresentation (38). Consequently, both deficiencies hampered Oxali- and Mito-induced H-2Kq mRNA and surface expression (Fig. 4H and SI Appendix, Fig. S6F-S6G). A p300/CBP inhibitor also attenuated H-2Kq protein, and *Psmb9* and *Tap1* mRNA inductions (SI Appendix, Fig. S6H-S6I). Conversely, treatment of Myc-CaP cells with non-lethal

doses of the HDACi panobinostat (LBH589) induced *Nlrc5*, *Psmb9*, and *Tap1* mRNAs and surface H-2Kq (SI Appendix, Fig. S6J-S6L).

To gather information about p300 and CBP in human cancer, we examined the TCGA data set and found significant correlations between *EP300* or *CBP* mRNAs and genes identified by our integrative RNA-seq and ATAC-seq analyses, including *RELA*, *STAT1*, *NFKB1*, *IFNGR2* and *NLRC5* (Fig. 5A-5B, and SI Appendix, Fig. S7A). Similar correlations were found between histone modifiers and genes involved in MHC-I AgPP and T cell inflammation, particularly in human liver cancer (SI Appendix, Fig. S7B-S7C). Cancers with *EP300/CBP* loss-of-function [LOF; deletion and/or copy number variants (CNV) loss] showed lower *ERAP1* and *IFNGR1* or HLA-A expression (Fig. 5B). Curiously, EP300 and CBP were described both as oncogenes and oncosuppressors (39, 40). Phenotypes associated with heterozygous alterations were described in B cell lymphoma and Rubinstein-Taybi syndrome-1 (41, 42), suggesting dosage-dependent EP300/CBP function. We found that multiple CNVs, both gains and losses, affected *EP300* and *CBP* in HCC (LIHC) and PCa (PRAD) (Fig. 5A, and SI Appendix, Table S1) and correlated with their expression (SI Appendix, Fig. S7D). Interestingly, increased *EP300* and *CBP* copy numbers correlated with improved LIHC patient survival (Fig. 5C). We also analyzed CNVs of genes involved in MHC-I AgPPM and IFN $\gamma$  signaling (Fig. 5D-5E, SI Appendix, Fig. S8A and Table S1). We found that LIHC and PRAD patients with gains in MHC-I AgPPM genes showed more frequent *EP300/CBP* LOF (Fig. 5D-5E, SI Appendix, Table S1), suggesting a compensatory mechanism that allows cancers with elevated MHC-I AgPPM evade immune-recognition. We also analyzed the number and the fraction of neoantigens in different cancers (SI Appendix, Fig. S8B-S8C). Remarkably, cancers with *EP300/CBP* LOF showed higher neoantigen amount (Fig. 5F and SI Appendix, Fig. S8D), supporting the notion that tumor immunoediting shapes the neoantigen landscape (43, 44) and that EP300/CBP may be part of this process.

### NF- $\kappa$ B signaling and MHC-I AgPPM induction

Electron microscopy (EM) suggested that Oxali-treated cells underwent nucleolar/ribosomal and mitochondrial stress indicated by the condensed appearance of both organelles (Fig. 6A-6B, and SI Appendix, Fig. S9A). However, the absence of nuclear or mitochondrial fragmentation confirmed that most of the stressed cells remained viable. Oxali-induced nucleolar/ribosomal stress (45, 46), which was confirmed by Mass Spectrometry (MS) and RNA-seq analyses (SI Appendix, Fig. S9B-S9E), can account for NF- $\kappa$ B activation (47). To determine NF- $\kappa$ B's role in the response to Oxali, we generated *RELA/p65*-deficient cell lines (SI Appendix, Fig. S10A-S10B). Consistent with the ChIP experiments shown above (Fig. 3E), *RELA/p65* was needed for full induction of *Ifngr2*, *Tap1*, *Psmab9*, *Nlrc5* and *Bat3* mRNAs by low dose Oxali (Fig. 6C-6E, and SI Appendix, Fig. S10C-S10D). *RELA/p65* ablation strongly inhibited surface H-2Kq induction by Oxali but barely affected the response to IFN $\gamma$  (Fig. 6F). *BAT3* and p300 nuclear translocation was also attenuated in *RELA*-deficient cells (Fig. 6G, and SI Appendix, Fig. S10E). Treatment of Myc-CaP cells with IKK $\beta$  inhibitors also reduced H-2Kq surface expression (SI Appendix, Fig. S10F). We also generated *IRF1*, *STING/cGAS*, *STAT1*, *IFN $\gamma$ R2* and *VDAC1* deficient Myc-CaP cells (Fig. 6H and SI Appendix, Fig. S11A-S11E). *VDAC1* (voltage dependent anion channel 1) was recently shown to be required for the cytoplasmic release of mitochondrial (mt) DNA (48), which is considerably elevated in Oxali-stressed cells (SI Appendix, Fig. S11E-S11F). Notably, *VDAC-1* ablation strongly reduced *Rela*, *p300* and *Irf-1* mRNA induction by Oxali (SI Appendix, Fig. S11G). Ablation of *VDAC1* and *IRF1*, but not *STAT1* or *IFN $\gamma$ R2* abrogated Oxali-induced expression of surface H-2Kq and MHC-I AgPPM genes (Fig. 6H, and SI Appendix, Fig. S11H-S11K). Ablation of *cGAS* led to a small decrease in H-2Kq expression and no effect on induction of most AgPPM genes (Fig. 6H, and SI Appendix, Fig. S11H-S11K). Not surprisingly, *STAT1*, *IRF-1* and *IFN $\gamma$ R2* as well as *VDAC1* and *cGAS* were required for H-2Kq surface expression in Myc-CaP cells treated with IFN $\gamma$  alone or IFN $\gamma$  + Oxali (SI Appendix, Fig. S11L). Oxali treatment also led to modest induction of PD-L1, a response that was enhanced by exogenous IFN $\gamma$



and was IRF1-dependent (SI Appendix, Fig. S11M), which has previously been shown to contribute to efficacy of ICIT (49). PD-L1 induction was not affected by TAP1 ablation, which completely prevented H-2Kq surface expression.

### **Chemotherapy induced functional antigen presentation**

To confirm that Oxali stimulates neoantigen presentation we used MS to determine the peptidomes of H-2Kb and H-2Db molecules isolated from MC-38 cells after treatments, as described previously (50). Treatment with IFN $\gamma$  + Oxali induced higher amounts (based on area under the curve) of H-2Kb-bound peptides relative to Oxali or IFN $\gamma$  alone (SI Appendix, Fig. S12A). Although IFN $\gamma$  led to higher amounts of H-2Db-bound peptides than Oxali in this particular cell line, chosen for its high MHC-I expression, some peptides were more efficiently presented after IFN $\gamma$  + Oxali treatment.

The T cell activating ability of the Oxali-induced MHC-I bound peptides was confirmed using TRC2 PCa cells expressing high-, medium-, and low-affinity ovalbumin (Ova) variants. Oxali treatment stimulated H-2Kb presentation of the SIINFEKL epitope, especially in TRC2-N4 cells made to express the high-affinity (WT) variant (SI Appendix, Fig. S12B). When incubated with OT-I CD8<sup>+</sup> T cells, whose T-cell receptor (TCR) is SIINFEKL-specific, Oxali treated TRC2-N4 cells were more readily killed by activated OT-I T cells (SI Appendix, Fig. S12C-S12D). OT-I T cells enhanced presentation of the WT SIINFEKL epitope by TRC2-N4 cells in the absence of Oxali but had no effect on cells expressing the medium (TRC2-G4)- or low (TRC2-E1)-affinity variants. These results are consistent with a previous publication showing that only the high-affinity SIINFEKL epitope induces IFN $\gamma$  secretion by OT-I cells (51), and further establish that the effect of Oxali is mechanistically distinct from that of IFN $\gamma$  and dependent on neoantigen affinity and TCR activation.

We examined mouse and human cancer cell lines that differ in basal MHC-I expression. As described above, cells with high basal MHC-I such as MC-38 and B16 melanoma showed a weak response to platinoids alone but that response, including *Nlrc5* mRNA and surface MHC-I, was augmented by IFN $\gamma$  (SI Appendix, Fig. S13A-S13B). In other cancer cells, e.g. the mouse melanoma YUMM cell lines, we observed a considerable variation in the response (SI Appendix, Fig. S13C). Strong Oxali-induced MHC-I surface expression was detected in human PC3 PCa cell line, PCSD1 cells, a 3D organoid culture from a Patient-Derived Xenograft (PDX) of bone metastatic PCa, certain primary melanoma cells and MIA PaCa-2 cells, representing ICIT-refractory PDAC (SI Appendix, Fig. S13D-S13G).

### **Activation of p300/CBP and NF- $\kappa$ B is needed for Oxali + anti-PD-L1 synergy**

We sorted tumor-infiltrating CD8<sup>+</sup> T cells (TI-CD8<sup>+</sup>) from subcutaneous (s.c.) Myc-CaP tumors, treated with either Oxali, anti-PD-L1, Oxali + anti-PD-L1 (combo) or left untreated (Ctrl) and performed scRNA-seq (Fig. 7A, SI Appendix, Fig. S14A). Several clusters of TI-CD8<sup>+</sup> cells with distinguishable gene expression and cluster specific pathway enrichment patterns were detected (Fig. 7B, and SI Appendix, Fig. S14B-S14H). Notably, elevated *Gzmb*, *Gzam*, *Prf1*, *Tbx21* (*Tbet*) mRNAs were detected in TI-CD8<sup>+</sup> from combo-treated mice (SI Appendix, Fig. S14E). Only combo therapy was associated with a significantly higher Teff signature (Fig. 7C and SI Appendix, Fig. S14F-S14H).

Next, we examined the involvement p300, CBP, IFN $\gamma$ R2 and NF- $\kappa$ B/RelA in Oxali-enhanced and CTL-mediated rejection of Myc-CaP tumors (Fig. 7A). The synergistic inhibition of tumor growth by Oxali + anti-PD-L1 was completely abrogated by p300 and CBP ablation in Myc-CaP cells (Fig. 7D-7G, and SI Appendix, Fig. S15A). IFN $\gamma$ R2 ablation also abolished the response to Oxali + anti-PD-L1 (Fig. 7G-7H and SI Appendix, Fig. S15B). As found in vitro, low-dose Oxali induced expression of *Ifngr2*, *Tap1*, *Psmb9*, and *Nlrc5* mRNA in Myc-CaP tumors (Fig. 7I-7K and SI Appendix, Fig. S15C). PD-L1 blockade did not affect *Ifngr2* mRNA expression, although it potentiated *Tap1*, *Psmb9*, and *Nlrc5* mRNA induction by Oxali, probably through IFN $\gamma$  secretion by reinvigorated CTLs (Fig. 7I-7K and SI Appendix, Fig. S15C).

Indeed, IFN $\gamma$ R2 ablation had little effect on the response to Oxali alone while abrogating the response to Oxali + anti-PD-L1. *Tap1*, *Psmb9*, and *Nlrc5* induction by Oxali or Oxali + anti-PD-L1 was abrogated after p300 ablation (Fig. 7I-7K). IFN $\gamma$ R2 and p300 ablation also attenuated therapy-induced MHC-I (H-2Kq and H-2Dd) surface expression on CD45 $^{-}$  cancer cells (Fig. 7L, and [SI Appendix, Fig. S15D-S15E](#)), but had no effect on PD-L1 expression ([SI Appendix, Fig. S15F](#)). IFN $\gamma$ R2 and p300 ablations also had no effect on H-2Kq expression by tumor-infiltrating CD11c $^{+}$  dendritic cells ([SI Appendix, Fig. S15G](#)). In accordance with scRNA-seq data, the Oxali+anti-PD-L1 combo increased the percentage and/or total numbers of tumor-infiltrating CD8 $^{+}$  and CD4 $^{+}$  T cells, CD107 $^{+}$ IFN $\gamma^{+}$  CTLs, IFN $\gamma^{+}$  CD8 $^{+}$  and TNF $^{+}$ IFN $\gamma^{+}$  CD8 $^{+}$  T cells, CD8 $^{+}$ CD44 $^{+}$  T eff cells and CD8 $^{+}$ CD44 $^{+}$ PD1 $^{+}$ TIM-3 $^{-}$  T cells analyzed by flow cytometry (Fig. 7M-7N and [SI Appendix, Fig. S16A, S16C-S16H](#)). Similar results were obtained for splenic CD8 $^{+}$  T cells ([SI Appendix, Fig. S16B, and S16I-S16K](#)). Of note, p300 or IFN $\gamma$ R2 ablation had little effect on tumor infiltrating effector CD8 $^{+}$  T cells, whose numbers were similarly increased after Oxali + anti-PD-L1 treatment in p300- or IFN $\gamma$ R2-expressing and non-expressing tumors (Fig. 7M-7N, and [SI Appendix, Fig. S16C-S16H](#)). By contrast, the Oxali + anti-PD-L1 combo decreased the fractions of each tumor occupied by CD45 $^{-}$  “cancer” cells, an effect that was most pronounced in WT tumors relative to p300 or IFN $\gamma$ R2 ablated tumors (Fig. 7O). NF- $\kappa$ B/RelA ablation also abolished the response to Oxali + anti-PD-L1 (Fig. 8A), consistent with its requirement for MHC-I and IFN $\gamma$ R2 induction (Fig. 8B, and [SI Appendix, Fig. S17A](#)). Thus, Oxali-induced upregulation of MHC-I AgPPM genes in malignant cells is important for the final recognition and killing stage of the cancer-immunity cycle (25) but has no role in ICIT-induced CTL reinvigoration.

Of note, ICD-mediated T cell priming proceeded normally in the absence of p300. FVB mice were immunized with Oxali-killed p300-proficient or -deficient Myc-CaP cells and challenged one week later with vital p300-proficient or -deficient Myc-CaP cells (Fig. 8C and [SI Appendix, Fig. S17B](#)). Myc-CaP cells grew significantly slower in FVB mice immunized with either p300-proficient or -deficient Myc-CaP cells compared to non-vaccinated mice, indicating that p300 has no effect on ICD-mediated T cell priming.

## Discussion

ICIT-induced tumor rejection depends on activation of the cancer-immunity cycle, initiated by priming of tumor-directed T cells and terminated by killing of the targeted cancer cells by effector CTLs (16, 25). T cell priming can be enhanced by certain chemotherapeutic drugs capable of inducing ICD (14) and ICIT (4, 27). Nonetheless, even highly effective T cell priming and ICIT do not ensure successful CTL-mediated tumor killing, which requires MHC-I mediated presentation of tumor specific antigens (2, 14, 17, 52). Many cancers, especially PCa ([SI Appendix, Fig. S7E](#)) (53), evade immune elimination by downregulating MHC-I molecules or essential AgPPM components (11). Here we show that two different chemotherapeutic drugs, oxaliplatin (Oxali) and mitoxantrone (Mito) used at rather low concentrations, enhance CTL-mediated cancer cell recognition and killing through transcriptional induction of MHC-I AgPP (Schematic summary, [SI Appendix, Fig. S17C](#)). Although induction of MHC-I antigen presentation by chemotherapy and radiotherapy was described (54–56), the underlying mechanisms were only partly explored and attributed to type I IFN signaling. However, recent reports showing that sustained type I IFN signaling contributes to anti-PD-(L)1 resistance (57, 58) cast doubt on the role played by type I IFN in chemotherapy or radiotherapy induced immune stimulation. Our results show that Oxali renders low MHC-I expressing PCa cells responsive to anti-PD-1 therapy through transcriptional activation of the MHC-I AgPPM by NF- $\kappa$ B and p300/CBP, but not via the IFN-responsive TF STAT1. Ablation of p300 (or CBP) or NF- $\kappa$ B/RelA abolished the ability of low dose Oxali to synergize with anti-PD-L1 and induce rejection of Myc-CaP tumors. Consistent with their direct involvement in transcriptional activation of MHC-I AgPPM genes, ablation of p300 or RelA abrogated *Tap1*, *Psmb9* and *Nlrc5* induction in Myc-CaP tumors, but had no effect on tumor infiltration by effector CD8 $^{+}$  cells. Tumor infiltrating CTLs, however, were strongly increased after anti-PD-L1 + Oxali treatment as indicated by scRNA-seq and flow

cytometry. In contrast, ablation of p300 had no effect on the ability of Oxali-killed Myc-CaP cells to prime anti-tumor immunity, as indicated by vaccination experiments.

Oxali treatment triggers nucleolar/ribosomal stress (45, 46), possibly through its preferential interaction with rDNA or inhibition of rRNA synthesis, which represents almost half of the human genome (59). By virtue of its highly repetitive nature, rRNA integrity and expression are also sensitive to loss of topoisomerase II activity (60), a sequelae of Mito treatment. EM analysis of Oxali treated Myc-CaP cells confirmed altered nucleolar morphology, consistent with nucleolar stress, which can trigger NF- $\kappa$ B activation (47). By inducing *Bat3* transcription, RelA/NF- $\kappa$ B supports p300/CBP nuclear translocation, further increasing its own activity and stimulating histone acetylation. Oxali treatment can also enhance NF- $\kappa$ B activity via mitochondrial stress, whose presence in Myc-CaP cells is suggested by increased mitochondrial density and appearance of fragmented mtDNA in the cytosol. Ablation of VDAC1, through which mtDNA exits the mitochondrion (48), reduced *p300* and *Rela* mRNA expression and abrogated induction of NLRC5 and different MHC-I AgPPM components. NF- $\kappa$ B is also needed for induction of IFN $\gamma$ R2. Although IFN $\gamma$ R2 ablation had no effect on Oxali-induced MHC-I surface expression in cultured cells, it abrogated the rejection of Myc-CaP tumors and inhibited induction of MHC-I AgPPM genes in mice treated with anti-PD-L1 + Oxali. We postulate that IFN $\gamma$ R2 induction in Myc-CaP cells makes them more responsive to IFN $\gamma$  secreted by tumor infiltrating CTL.

Neither Oxali nor Mito were developed as immunostimulatory drugs. It is therefore understandable that their immunogenic activity depends on multiple signaling pathways that are activated on induction of sub-lethal DNA damage and nucleolar and mitochondrial stress. Given the number of different signaling pathways activated by Oxali or Mito, it is rather surprising that ablation of either p300/CBP or RelA results in almost complete inhibition of the drug-induced immunogenic response. These findings parallel the cardinal importance of p300/CBP and NF- $\kappa$ B in activation of the MHC-I AgPP system. p300 plays a key role in assembly of the NLRC5 transcriptional activation complex and NF- $\kappa$ B recruitment to MHC-I genes (61). Notably, downregulation of NLRC5 has been observed in multiple cancer types, resulting in evasion of immune elimination (12). Conversely, we found that cancers with NLRC5 gain were more likely to undergo *CPB/EP300* loss. We also found that *EP300* and *CBP* LOF mutations and CNVs are rather common in certain types of cancer, and that their presence correlates with reduced MHC-I AgPPM expression. These genetic alterations seem more common than HLA loss mutations. Moreover, HCC and PCa with gain of *HLA*, *PSMB* and *TAP* genes, possibly due to chromosome 6p amplification (62), show higher frequency of *CBP/EP300* loss, which may allow them to undergo immune evasion. Based on its loss in several types of cancer, *EP300* was suggested to behave as a tumor suppressor gene (63, 64). We suggest that *CBP/EP300* loss promotes tumor growth by enabling immune evasion. One way to restore recognition of tumors with monoallelic *EP300/CBP* loss is treatment with low-dose Oxali or Mito or more potent and specific EP300/CBP activators.

## Material and Methods

Detailed information about the animal models, in-vivo and in-vitro studies, flow cytometry, qRT-PCR, Immunoblot analysis, bioinformatic analysis, statistics and materials is provided in [SI Appendix Material and Methods and Table S2](#).

### Data and Materials Availability

This study did not generate new unique materials. The Sequencing data are available in NCBI's Gene Expression Omnibus database. Mouse ATAC-seq (GSE126287) and RNA-seq (GSE126274). Single cell RNA-seq data from live CD8<sup>+</sup>CD3<sup>+</sup> tumor infiltrating cells are available under the GEO accession number GSE151611.

## Acknowledgements

We thank N.T. Ryujin, A. Perkins, C.R. Lichtenstern, T. Deerinck, M. Mackey, D.T. Tam, S. Lee, E. Sanchez-Lopez, S. Pandit, K. Wong, and M. Muldong for technical support and help, and A. Birmingham, L. Delamarre, E. Fokas and C.M. Rödel for discussion and advise. S.S. was supported by PCF-Young Investigator Award, Merck MISP 57917 and the NIAAA funded SCRC for ALPD & Cirrhosis (P50 AA011999). Work in M.K. laboratory was supported by grants from the NIH (AI043477, CA128814, CA211794), Tower Cancer Research Foundation and San Diego NCI Cancer Centers Council (C3) and Padres Pedal the Cause #PTC2018. Additional support came from U01AA027681 to S.S. and M.K., P01 CA128814 to M.K./Ze'ev Ronai and M.B., U24CA232979 to S.L., DP5-OD017937 to H.C., 111 project (B16021) to X.L., NIH National Library of Medicine Training Grant T15LM011271 to M.D. NIH grant UL1TR001442 of CTSA to K.F., NIH P41GM103412, R24GM137200 and S10OD021784 to MHE, Mary Kay Ash Breast Cancer grant 047.16 and MCC-award to S.B. (J. E. Dixon). The results shown here are in part based upon data generated by the TCGA Research Network: <https://www.cancer.gov/tcga>.

## REFERENCES

1. A. M. M. Eggermont, *et al.*, Adjuvant Pembrolizumab versus Placebo in Resected Stage III Melanoma. *N. Engl. J. Med.* **378**, 1789–1801 (2018).
2. L. Gandhi, *et al.*, Pembrolizumab plus Chemotherapy in Metastatic Non-Small-Cell Lung Cancer. *N. Engl. J. Med.* **378**, 2078–2092 (2018).
3. W. Hugo, *et al.*, Genomic and Transcriptomic Features of Response to Anti-PD-1 Therapy in Metastatic Melanoma. *Cell* **165**, 35–44 (2016).
4. J. J. Havel, D. Chowell, T. A. Chan, The evolving landscape of biomarkers for checkpoint inhibitor immunotherapy. *Nat. Rev. Cancer* **19**, 133–150 (2019).
5. F. Conforti, *et al.*, Cancer immunotherapy efficacy and patients' sex: a systematic review and meta-analysis. *Lancet Oncol.* **19**, 737–746 (2018).
6. S. Guo, M. Contratto, G. Miller, L. Leichman, J. Wu, Immunotherapy in pancreatic cancer: Unleash its potential through novel combinations. *World J. Clin. Oncol.* **8**, 230–240 (2017).
7. E. S. Antonarakis, *et al.*, Pembrolizumab for Treatment-Refractory Metastatic Castration-Resistant Prostate Cancer: Multicohort, Open-Label Phase II KEYNOTE-199 Study. *J. Clin. Oncol.* **38**, 395–405 (2020).
8. M. K. Hossain, K. Nahar, O. Donkor, V. Apostolopoulos, Immune-based therapies for metastatic prostate cancer: an update. *Immunotherapy* **10**, 283–298 (2018).
9. T. M. Beer, *et al.*, Randomized, Double-Blind, Phase III Trial of Ipilimumab Versus Placebo in Asymptomatic or Minimally Symptomatic Patients With Metastatic Chemotherapy-Naive Castration-Resistant Prostate Cancer. *J. Clin. Oncol. Off. J. Am. Soc. Clin. Oncol.* **35**, 40–47 (2017).
10. S. Mariathasan, *et al.*, TGF $\beta$  attenuates tumour response to PD-L1 blockade by contributing to exclusion of T cells. *Nature* **554**, 544–548 (2018).
11. D. Dersh, J. Hollý, J. W. Yewdell, A few good peptides: MHC class I-based cancer immunosurveillance and immunoevasion. *Nat. Rev. Immunol.*, 1–13 (2020).
12. S. Yoshihama, *et al.*, NLRC5/MHC class I transactivator is a target for immune evasion in cancer. *Proc. Natl. Acad. Sci.* **113**, 5999–6004 (2016).
13. T. N. Schumacher, W. Scheper, P. Kvistborg, Cancer Neoantigens. *Annu. Rev. Immunol.* **37**, 173–200 (2019).
14. L. Galluzzi, A. Buqué, O. Kepp, L. Zitvogel, G. Kroemer, Immunogenic cell death in cancer and infectious disease. *Nat. Rev. Immunol.* **17**, 97–111 (2017).
15. L. Galluzzi, *et al.*, Consensus guidelines for the definition, detection and interpretation of immunogenic cell death. *J. Immunother. Cancer* **8** (2020).
16. D. S. Chen, I. Mellman, Elements of cancer immunity and the cancer-immune set point. *Nature* **541**, 321–330 (2017).
17. D. Chowell, *et al.*, Evolutionary divergence of HLA class I genotype impacts efficacy of cancer immunotherapy. *Nat. Med.* **25**, 1715–1720 (2019).
18. S. Gettinger, *et al.*, Impaired HLA Class I Antigen Processing and Presentation as a Mechanism of Acquired Resistance to Immune Checkpoint Inhibitors in Lung Cancer. *Cancer Discov.* **7**, 1420–1435 (2017).
19. M. Šmahel, PD-1/PD-L1 Blockade Therapy for Tumors with Downregulated MHC Class I Expression. *Int. J. Mol. Sci.* **18** (2017).
20. N. Vitkin, S. Nersesian, D. R. Siemens, M. Koti, The Tumor Immune Contexture of Prostate Cancer. *Front. Immunol.* **10** (2019).
21. P. Cresswell, A. L. Ackerman, A. Giodini, D. R. Peaper, P. A. Wearsch, Mechanisms of MHC class I-restricted antigen processing and cross-presentation. *Immunol. Rev.* **207**, 145–157 (2005).
22. S. Shalapour, *et al.*, Immunosuppressive plasma cells impede T-cell-dependent immunogenic chemotherapy. *Nature* **521**, 94–98 (2015).
23. C. He, *et al.*, Core-shell nanoscale coordination polymers combine chemotherapy and photodynamic therapy to potentiate checkpoint blockade cancer immunotherapy. *Nat. Commun.* **7**, 12499 (2016).
24. C. Pfirschke, *et al.*, Immunogenic Chemotherapy Sensitizes Tumors to Checkpoint Blockade Therapy. *Immunity* **44**, 343–354 (2016).
25. D. S. Chen, I. Mellman, Oncology Meets Immunology: The Cancer-Immunity Cycle. *Immunity* **39**, 1–10 (2013).
26. J. D. Buenrostro, B. Wu, H. Y. Chang, W. J. Greenleaf, ATAC-seq: A Method for Assaying Chromatin Accessibility Genome-Wide. *Curr. Protoc. Mol. Biol.* **109**, 21.29.1–9 (2015).



27. S. C. Wei, C. R. Duffy, J. P. Allison, Fundamental Mechanisms of Immune Checkpoint Blockade Therapy. *Cancer Discov.* **8**, 1069–1086 (2018).
28. N. Karachaliou, *et al.*, Interferon gamma, an important marker of response to immune checkpoint blockade in non-small cell lung cancer and melanoma patients. *Ther. Adv. Med. Oncol.* **10** (2018).
29. T. A. Hore, J. E. Deakin, J. A. Marshall Graves, The Evolution of Epigenetic Regulators CTCF and BORIS/CTCF in Amniotes. *PLoS Genet.* **4**, e1000169 (2008).
30. D. Bernard, A. Pourtier-Manzanedo, J. Gil, D. H. Beach, Myc confers androgen-independent prostate cancer cell growth. *J. Clin. Invest.* **112**, 1724–1731 (2003).
31. C. M. Koh, *et al.*, MYC and Prostate Cancer. *Genes Cancer* **1**, 617–628 (2010).
32. C. A. Heinlein, C. Chang, Androgen Receptor in Prostate Cancer. *Endocr. Rev.* **25**, 276–308 (2004).
33. Q. Qin, *et al.*, Lisa: inferring transcriptional regulators through integrative modeling of public chromatin accessibility and ChIP-seq data. *Genome Biol.* **21**, 32 (2020).
34. R. Janky, *et al.*, iRegulon: From a Gene List to a Gene Regulatory Network Using Large Motif and Track Collections. *PLoS Comput. Biol.* **10**, e1003731 (2014).
35. M. D. Shahbazian, M. Grunstein, Functions of Site-Specific Histone Acetylation and Deacetylation. *Annu. Rev. Biochem.* **76**, 75–100 (2007).
36. E. Ortega, *et al.*, Transcription factor dimerization activates the p300 acetyltransferase. *Nature* **562**, 538–544 (2019).
37. S. Sebti, *et al.*, BAT3 modulates p300-dependent acetylation of p53 and autophagy-related protein 7 (ATG7) during autophagy. *Proc. Natl. Acad. Sci. U. S. A.* **111**, 4115–4120 (2014).
38. I. Cebrian, *et al.*, Sec22b Regulates Phagosomal Maturation and Antigen Crosspresentation by Dendritic Cells. *Cell* **147**, 1355–1368 (2011).
39. R. H. Goodman, S. Smolik, CBP/p300 in cell growth, transformation, and development. *Genes Dev.* **14**, 1553–1577 (2000).
40. N. G. Iyer, H. Özdag, C. Caldas, p300/CBP and cancer. *Oncogene* **23**, 4225–4231 (2004).
41. J. H. Roelfsema, *et al.*, Genetic Heterogeneity in Rubinstein-Taybi Syndrome: Mutations in Both the CBP and EP300 Genes Cause Disease. *Am. J. Hum. Genet.* **76**, 572–580 (2005).
42. J. Zhang, *et al.*, The Crebbp acetyltransferase is a haploinsufficient tumor suppressor in B cell lymphoma. *Cancer Discov.* **7**, 322–337 (2017).
43. R. Marty, *et al.*, MHC-I Genotype Restricts the Oncogenic Mutational Landscape. *Cell* **171**, 1272–1283.e15 (2017).
44. A. Castro, *et al.*, Elevated neoantigen levels in tumors with somatic mutations in the HLA-A, HLA-B, HLA-C and B2M genes. *BMC Med. Genomics* **12**, 107 (2019).
45. P. M. Bruno, *et al.*, A subset of platinum-containing chemotherapeutic agents kills cells by inducing ribosome biogenesis stress. *Nat. Med.* **23**, 461–471 (2017).
46. T. Ozdian, *et al.*, Proteomic profiling reveals DNA damage, nucleolar and ribosomal stress are the main responses to oxaliplatin treatment in cancer cells. *J. Proteomics* **162**, 73–85 (2017).
47. J. Chen, L. A. Stark, Insights into the Relationship between Nucleolar Stress and the NF-κB Pathway. *Trends Genet.* **35**, 768–780 (2019).
48. J. Kim, *et al.*, VDAC oligomers form mitochondrial pores to release mtDNA fragments and promote lupus-like disease. *Science* **366**, 1531–1536 (2019).
49. H. Lin, *et al.*, Host expression of PD-L1 determines efficacy of PD-L1 pathway blockade-mediated tumor regression. *J. Clin. Invest.* **128**, 805–815 (2018).
50. M. Yadav, *et al.*, Predicting immunogenic tumour mutations by combining mass spectrometry and exome sequencing. *Nature* **515**, 572–576 (2014).
51. A. E. Denton, *et al.*, Affinity Thresholds for Naive CD8+ CTL Activation by Peptides and Engineered Influenza A Viruses. *J. Immunol.* **187**, 5733–5744 (2011).
52. C. J. Langer, *et al.*, Carboplatin and pemetrexed with or without pembrolizumab for advanced, non-squamous non-small-cell lung cancer: a randomised, phase 2 cohort of the open-label KEYNOTE-021 study. *Lancet Oncol.* **17**, 1497–1508 (2016).
53. E. B. Ylitalo, *et al.*, Subgroups of Castration-resistant Prostate Cancer Bone Metastases Defined Through an Inverse Relationship Between Androgen Receptor Activity and Immune Response. *Eur. Urol.* **71**, 776–787 (2017).



54. A. R. de Biasi, J. Villena-Vargas, P. S. Adusumilli, Cisplatin-induced antitumor immunomodulation: a review of preclinical and clinical evidence. *Clin. Cancer Res. Off. J. Am. Assoc. Cancer Res.* **20**, 5384–5391 (2014).
55. H. Khallouf, *et al.*, 5-Fluorouracil and Interferon- $\alpha$  Immunochemotherapy Enhances Immunogenicity of Murine Pancreatic Cancer Through Upregulation of NKG2D Ligands and MHC Class I. *J. Immunother.* **35**, 245–253 (2012).
56. S. Wan, *et al.*, Chemotherapeutics and Radiation Stimulate MHC Class I Expression through Elevated Interferon-beta Signaling in Breast Cancer Cells. *PLoS ONE* **7** (2012).
57. J. Chen, *et al.*, Type I IFN protects cancer cells from CD8+ T cell-mediated cytotoxicity after radiation. *J. Clin. Invest.* **129**, 4224–4238 (2019).
58. N. Jacquelot, *et al.*, Sustained Type I interferon signaling as a mechanism of resistance to PD-1 blockade. *Cell Res.* **29**, 846–861 (2019).
59. D. O. Warmerdam, R. M. F. Wolthuis, Keeping ribosomal DNA intact: a repeating challenge. *Chromosome Res.* **27**, 57–72 (2019).
60. S. L. French, *et al.*, Distinguishing the Roles of Topoisomerases I and II in Relief of Transcription-Induced Torsional Stress in Yeast rRNA Genes. *Mol. Cell. Biol.* **31**, 482–494 (2011).
61. T. B. Meissner, *et al.*, NLRC5 cooperates with the RFX transcription factor complex to induce MHC class I gene expression. *J. Immunol.* **188**, 4951–4958 (2012).
62. G. C. Santos, M. Zielenska, M. Prasad, J. A. Squire, Chromosome 6p amplification and cancer progression. *J. Clin. Pathol.* **60**, 1–7 (2007).
63. N. Attar, S. K. Kurdistani, Exploitation of EP300 and CREBBP Lysine Acetyltransferases by Cancer. *Cold Spring Harb. Perspect. Med.* **7** (2017).
64. S. A. Gayther, *et al.*, Mutations truncating the EP300 acetylase in human cancers. *Nat. Genet.* **24**, 300–303 (2000).

## Figure legends

**Fig. 1.** Chemotherapy induces MHC-I AgPPM genes. (A) Heatmap showing all DEGs identified in bulk RNAseq of Myc-CaP cells treated with IFN $\gamma$  (0.2 or 2 ng/mL), Oxali (2  $\mu$ M), or both (Combo) (left). Venn diagram shows overlapping DEGs between IFN $\gamma$  (2 ng/mL), Oxali and Combo treatment groups relative to Ctrl (middle) and Heatmap shows all DARs identified in bulk ATAC-seq of Myc-CaP cells treated as indicated relative to control (right). (B) GSEA was applied to expression profiles specific to each treatment group relative to Ctrl. Top 30 significantly enriched pathways for each respective comparison are shown. Some pathways were considered both IFN $\gamma$  and Oxali driven (purple), while others were specific to either IFN $\gamma$  (blue) or Oxali (red). (C) Functional enrichment was applied to genes classified with additive response to combination therapy. The top 20 enriched REACTOME pathways are shown.

**Fig. 2.** Transcriptional regulators of Oxali-induced MHC-I AgPPM genes. (A) RNAs from Myc-CaP cells incubated as indicated with IFN $\gamma$ , Mito, Oxali, Carbo, or Cispl for 48 h were analyzed by qRT-PCR using *Nirc5* primers. (B-C) Candidate genomic loci for *Nirc5* (B) and *Ifngr2* (C), showing library-size normalized read pair pileup profiles determined by ATAC-seq across samples. Expression of respective genes determined by RNA-seq is also shown. (D) RNAs from Myc-CaP cells incubated as indicated were analyzed by qRT-PCR using *Ifngr2* primers. (E) Myc-CaP cells incubated with Oxali for 12 h were stained with  $\beta$ 2M antibody (green) and phalloidin (red) and counterstained with DAPI. Magnification bar: 20  $\mu$ m. (F) Myc-CaP cells treated as indicated were analyzed for surface MHC-I (H-2Kq) expression by flow cytometry. One-way ANOVA analysis (\*\*\*) and multiple comparison confirmed the results. (G) Myc-CaP cells were incubated as indicated and lysed. LMP7 (PSMB8) immunoproteasome activity was measured using a fluorogenic LMP7-specific substrate peptide Ac-ANW-AMC. (H) Candidate genomic locus for *Nfkb1* showing read density profiles determined by ATAC-seq across samples. (I) Transcriptional regulator inference analysis (LISA) was applied to DEGs identified in comparisons of IFN $\gamma$  (2 ng/mL), Oxali (2  $\mu$ M), and both (Combo) treated cells relative to control, as well as to genes classified with additive response (top 500 upregulated, downregulated DEGs). The top 20 enriched regulators of upregulated (red) and downregulated (blue) DEGs are noted. (J) Transcriptional regulator binding sites enrichment analysis (GIGGLE) was applied to DARs identified in comparisons of IFN $\gamma$ , Oxali, and Combo treated cells relative to control, as well as to regions classified with additive response. The top 20 enriched regulators of opened (red) and closed (blue) DARs are noted. (K) 200 common genes were identified by comparing TF found by DEGs and DARs analysis. (L) GSEA was applied to expression profiles determined in Oxali treated cells relative to control. The literature-curated known regulatory elements from ORegAnno database are shown. Candidate enrichment plots for representative pathways related to histone methylation (top) and acetylation (bottom) are shown. Two-sided t-test (means  $\pm$  s.e.m), and Mann-Whitney test (median) were used to determine significance between two-groups. One-way ANOVA analysis and multiple comparison confirmed the results. \*P < 0.05; \*\*P < 0.01; \*\*\*P < 0.001; NS, not significant. Specific n values are shown in (A, D, F, G), each experiment includes at least three biological replicates.

**Fig. 3.** Oxaliplatin and mitoxantrone stimulate HAT activity and nuclear localization. (A-B) Myc-CaP cells incubated with Oxali (2 or 4  $\mu$ M) or the HDACi panobinostat (LBH589; 20 nM) for the

indicated times were lysed and analyzed for HAT activity using H3 as a substrate. (C) Nuclear extracts of Myc-CaP cells treated with Oxali, Mito and/or IFN $\gamma$  were IB analyzed for p300, acetylated-CBP/p300, acetylated-RELA/p65 (lysine K310) and lamin B1 (loading control). (D) Myc-CaP cells treated as indicated for 12 h were stained with anti p300 (green) and phalloidin (red; actin cables). Nuclei were counter stained with DAPI (blue). Magnification bar: 20  $\mu$ m. (E-G) Untreated and Oxali treated Myc-CaP cells were subjected to ChIP analysis with control IgG and antibodies to p65/RelA, p300 as indicated (E-F) or acetylated H3 (lysine K9, K14, and K27) (G). Precipitation of the indicated promoter regions was determined by PCR. Two-sided t-test (means  $\pm$  s.e.m), and Mann-Whitney test (median) were used to determine significance. \*P < 0.05; \*\*P < 0.01; \*\*\*P < 0.001; NS, not significant. Specific n values are shown in (A, E), each experiment includes at least three biological replicates.

**Fig. 4.** p300 and CBP control Oxali-induced MHC-I AgPPM genes. (A) Parental (shRNA-Ctrl) and *p300* or *CBP* silenced Myc-CaP cells were incubated with Oxali for 48 h. Nuclear extracts were IB analyzed for p300, CBP, p65/RELA and HDAC1 (loading control). (B-G) RNA expression in above cells was analyzed by qRT-PCR with the indicated primers. (H) Parental and gene edited Myc-CaP cells were incubated with Oxali and analyzed for surface MHC-I (H-2Kq) expression by flow cytometry. Two-sided t-test (means  $\pm$  s.e.m), and Mann-Whitney test (median) were used to determine significance unless indicated otherwise. \*P < 0.05; \*\*P < 0.01; \*\*\*P < 0.001; NS, not significant. Specific n values are shown in (B-H). Each experiment includes at least three biological replicates.

**Fig. 5.** p300/CBP control MHC-I AgPPM expression in human cancers. (A) *EP300* and *CBP* CNV losses and gains in LIHC (n = 369) and PRAD (n = 492). Key: dark blue (homozygous deletion), light blue (one copy loss), white (no CNV), pink (one copy gain), and red (high amplification). (B) Comparison of immune gene expression between LIHC *EP300/CBP* LOF and non-LOF groups. Non-viral patients are included for comparison of *CBP*, *EP300*, *ERAP1*, and *IFNGR1* expression. HLA-A expression was compared between *EP300/CBP* LOF and non-LOF HBV-infected groups. (C) Kaplan-Meier survival curves of LIHC patients with single gain (n = 34), no CNV (n = 165), and single loss (n = 92) events in *EP300/CBP*. P-values are based on log rank test. (D-E) Enrichment comparison of LIHC (D) and PRAD (E) with or without *EP300/CBP* LOF or no CNV versus CNV gain in the indicated gene groups: MHC-I AgPPM (HLA/PSMBs/TAPs), STAT1/IFNGR1/IFNGR2,  $\beta$ 2M and NLRC5. Fisher's exact test was used to determine significance. (F) Landscape of high affinity neoantigens in four tumor types: PRAD (n = 492), LIHC (n = 356), LUSC (n = 473), and SKCM (n = 445). Groups were separated into *EP300/CBP* LOF (green dots) and non-LOF for neoantigen analysis. Mutations receiving a rank score < 2 and < 0.5 were considered binding and strong binding, respectively. P-values are based on Wilcoxon rank-sum test. Expression of neoantigens was determined from TCGA mRNA-seq reads. Two-sided t-test (means  $\pm$  s.e.m), and Mann-Whitney test (median) were used to determine significance unless indicated otherwise. One-way ANOVA analysis and multiple comparison confirmed the results. \*P < 0.05; \*\*P < 0.01; \*\*\*P < 0.001; NS, not significant. Specific n values are shown in (A-F). Each experiment includes at least three biological replicates.

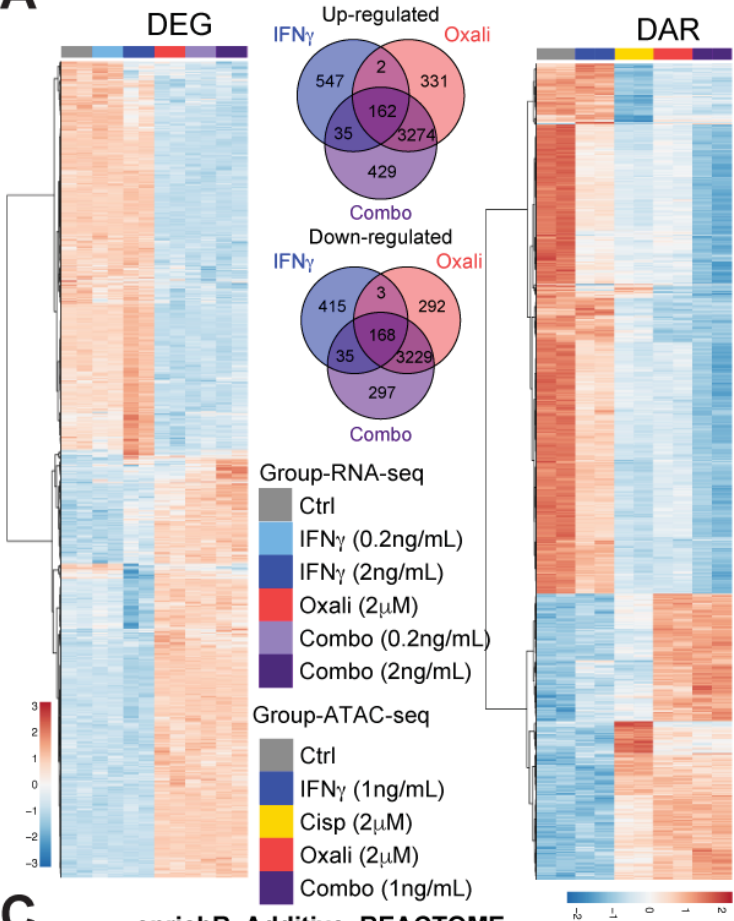
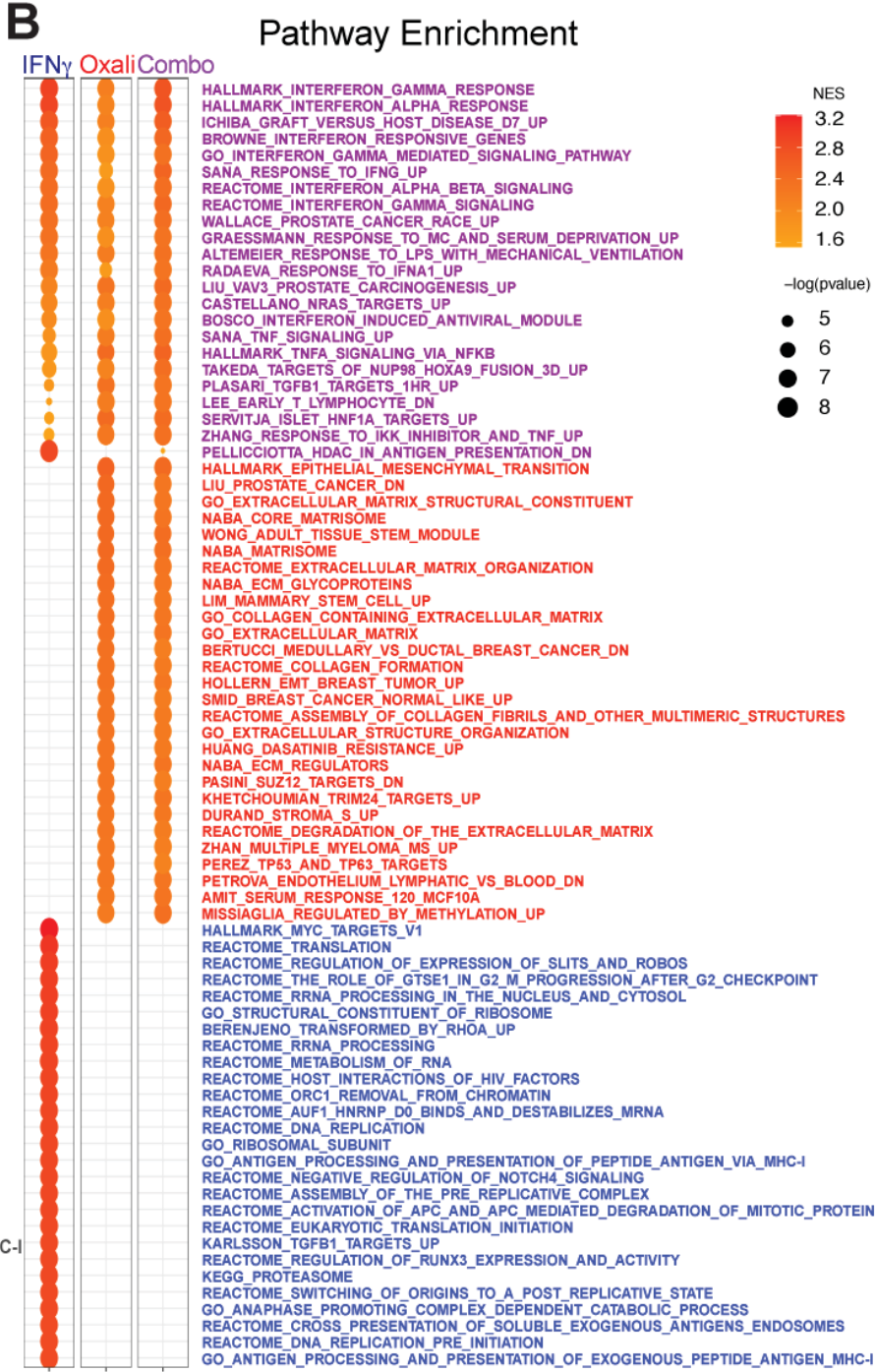
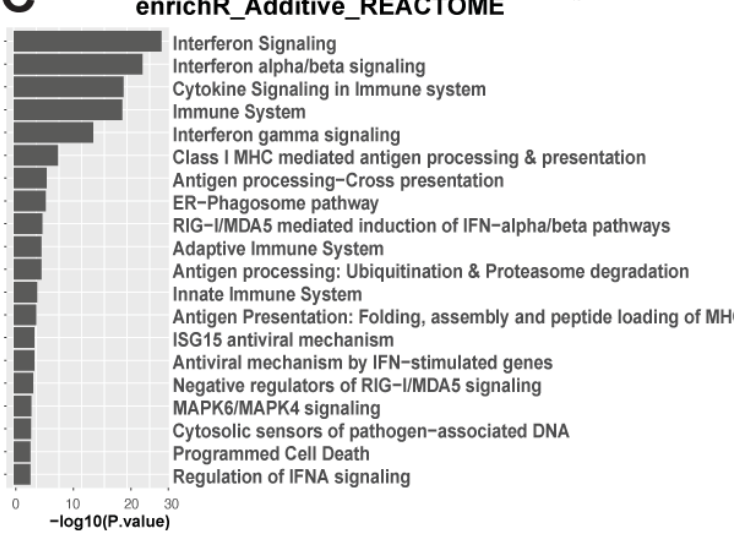
**Fig. 6.** Role of NF- $\kappa$ B signaling in Oxali-induced MHC-I AgPPM expression. (A, B) Myc-CaP cells treated as indicated were fixed and examined by electron microscopy. Magnification bars are indicated in each image. White arrows indicate nucleolar stress. 10 representative images from each treatment group were analyzed and mitochondria/cytoplasm ratios were determined (B, right). (C-E) Parental (shRNA-Ctrl) or *Rela/p65*-silenced Myc-CaP cells were incubated with Oxali as indicated. RNAs were analyzed by qRT-PCR with the indicated primers. The results were confirmed using three different *Rela/p65* shRNAs. (F) Myc-CaP cells described in (C) were treated as indicated and analyzed for surface MHC-I (H-2Kq) expression. (G) Parental or *Rela/p65*-silenced Myc-CaP cells were treated as indicated and stained with mouse-anti p300 (green) and rabbit-anti BAT3 (red). Nuclei were counterstained with DAPI (blue) (n = 3). Magnification bar: 20  $\mu$ m. (J) Parental and gene edited (Ctrl, CRISPR/Cas9) or shRNA silenced Myc-CaP cells were treated as indicated and analyzed for surface MHC-I (H-2Kq) expression. (B-F, H) Two-sided t-test (means  $\pm$  s.e.m), and Mann–Whitney test (median) were used to determine significance. One-way ANOVA and multiple comparisons were used to confirm significance. \*P < 0.05; \*\*P < 0.01; \*\*\*P < 0.001; NS, not significant. Specific n values are shown in (B-F). Each experiment includes at least three biological replicates.

**Fig. 7.** Oxali + anti-PD-L1 synergy depends on p300/CBP and IFN $\gamma$ R2 expression. (A) Schematic description of in vivo experiments. Mice bearing s.c. Myc-CaP tumors were allocated into 4 treatment groups: (1) Control, (2) Oxali (6 mg/kg; weekly), (3) anti-PD-L1 (10 mg/kg; weekly), and (4) Oxali + anti-PD-L1 (weekly). After 4 treatment cycles, during which tumor size was measured, the mice were euthanized and analyzed. (B) UMAP representation of total T cell populations profiled by scRNAseq. Eleven distinct clusters were identified (Figure S14B-S14C). Proportional contributions of each cluster to sample-specific T cell populations is shown. Total cell numbers in each cluster are noted in Figure S14D. (C) Enrichment plots for candidate pathways defining CD8<sup>+</sup> Teff over Tmem and Tnaïve cells. Enrichment plots for the comparison between control and combo treatment is shown (other comparisons are shown in S14H). (D-F, H) Mice bearing s.c. Myc-CaP tumors generated by control (D), *p300*-silenced (E-F), and *Ifngr2* ablated (Clone 1) (H) cells were treated as described in (A). Specific n values are shown in each panel. Transient Cas9 expression and stable shRNA transfectants were used to avoid immune responses. Each dot is a treatment group, mean  $\pm$  s.e.m. (G) Tumor weights for the indicated experimental groups (n = 3-8). (D-H) Two-sided t-test (means  $\pm$  s.e.m) and two-way ANOVA were used to determine significance. (I-K) Total tumor RNA was analyzed by qRT-PCR for expression of the indicated genes. (L-N) Single cell tumor suspensions were analyzed for H-2Kq (L) expression on CD45<sup>-</sup> cells, total number of TI-CD8<sup>+</sup> (M) and effector CD8<sup>+</sup>IFN $\gamma$ <sup>+</sup>CD107<sup>+</sup> T cell subsets (N). (O) Solid tumor composition (% cancer cells) was determined by gating on CD45<sup>-</sup> cells. (G, I-O) Each dot represents a mouse. Mann–Whitney test (median) was used to determine significance. One-way ANOVA and multiple comparisons were used to confirm significance. Specific n values are shown in D-O.

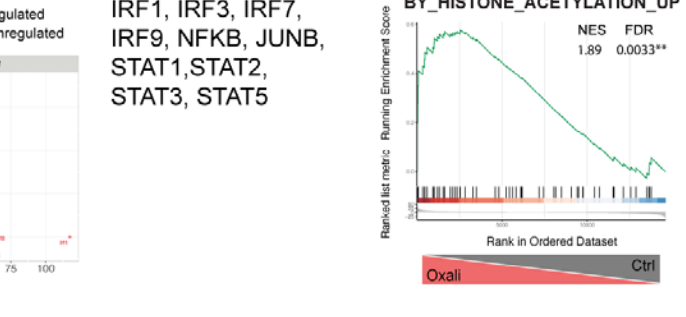
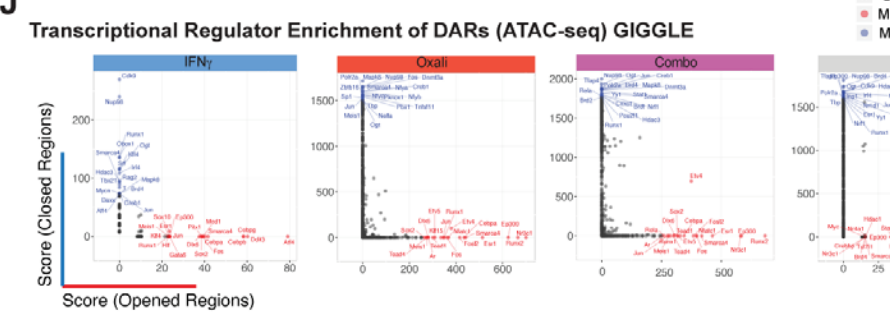
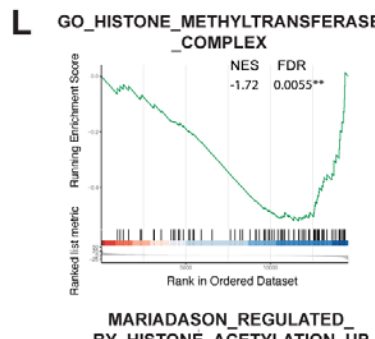
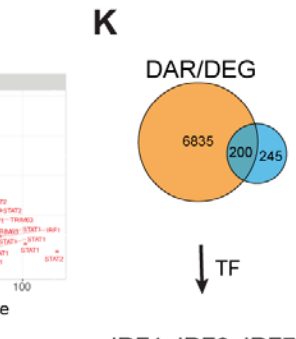
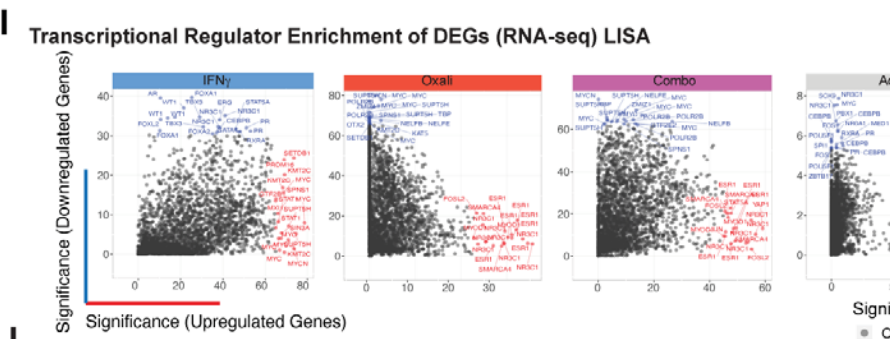
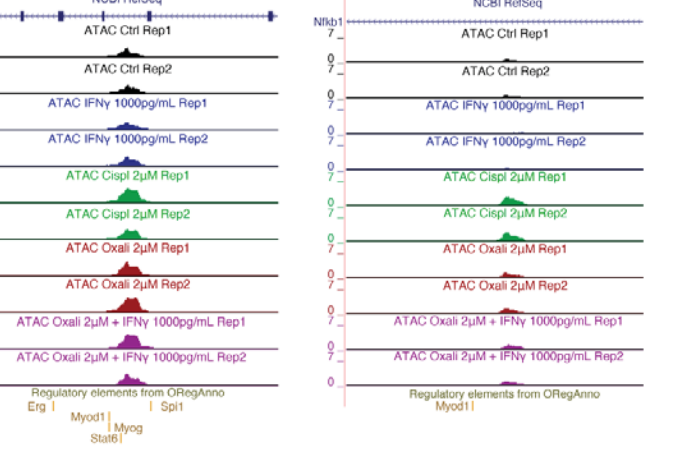
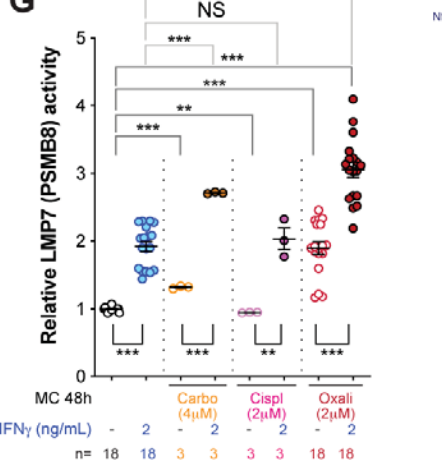
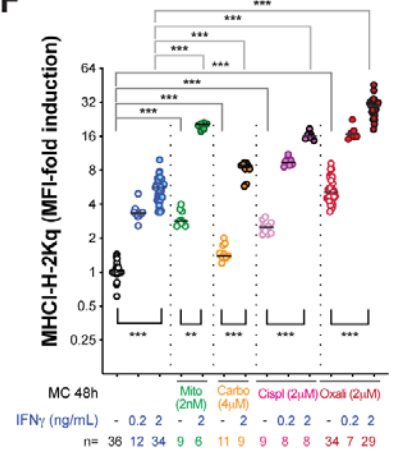
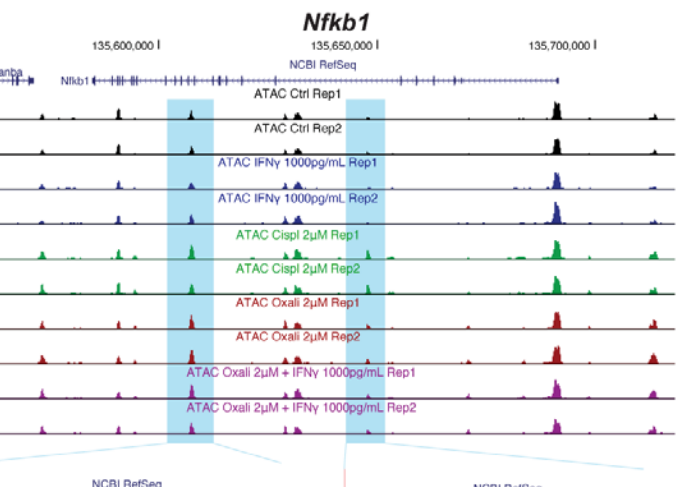
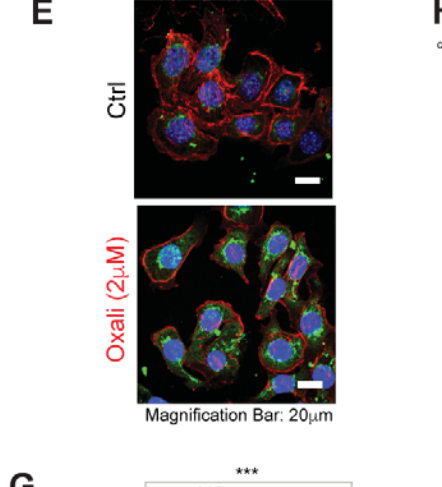
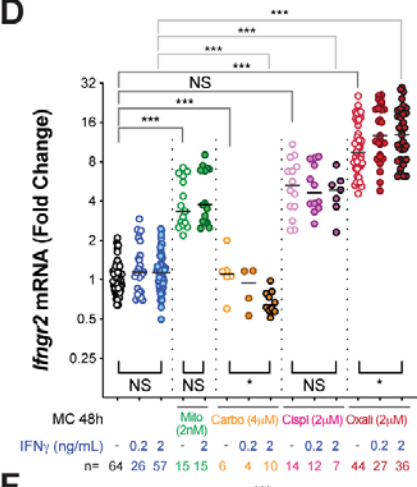
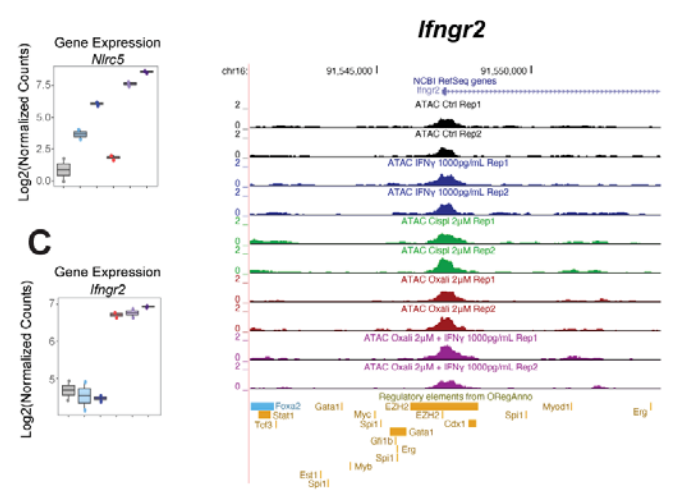
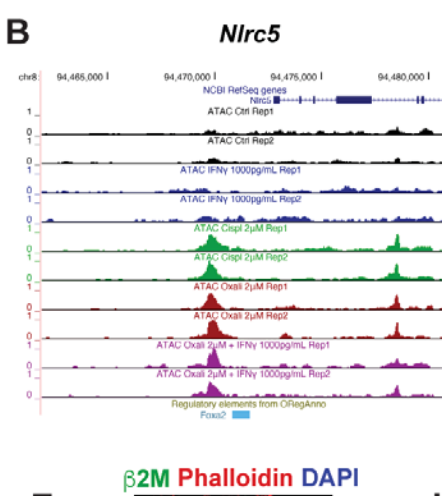
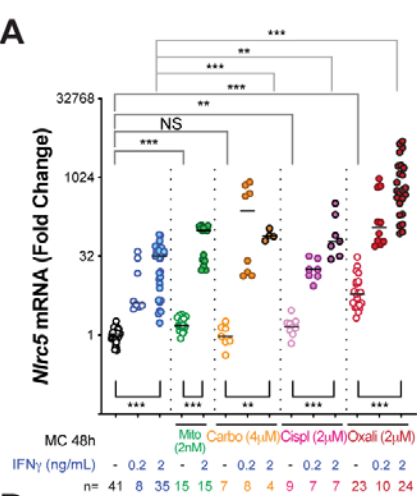
**Fig. 8.** Oxali-enhanced immune rejection requires NF- $\kappa$ B signaling. (A) Mice bearing s.c. Myc-CaP tumors generated by control and *RelA*-silenced cells were treated and analyzed as described in Figure 7A. Each dot represents a treatment group mean  $\pm$  s.e.m. (B) Single tumor cell suspensions were analyzed for H-2Kq (left) and H-2Dd (right) expression on CD45<sup>-</sup> cells. (C) Scheme of vaccination experiments (left). Two groups of mice were immunized with lysates of Oxali-killed shRNA-ctrl (MC<sup>wt</sup>) or *p300*-silenced (MC-*p300*<sup>Δ</sup>) Myc-CaP cells. After 7 days, mice were s.c. inoculated with live shRNA-ctrl (MC<sup>wt</sup>) cells. Live shRNA-ctrl (MC<sup>wt</sup>) cells were also implanted into non-immunized mice as a control. Tumor growth curves are shown (right).

(A-C) Two-sided t-test (means  $\pm$  s.e.m) and two-way ANOVA were used to determine significance. \*P < 0.05; \*\*P < 0.01; \*\*\*P < 0.001; NS, not significant. Specific *n* values are shown in (A-C).

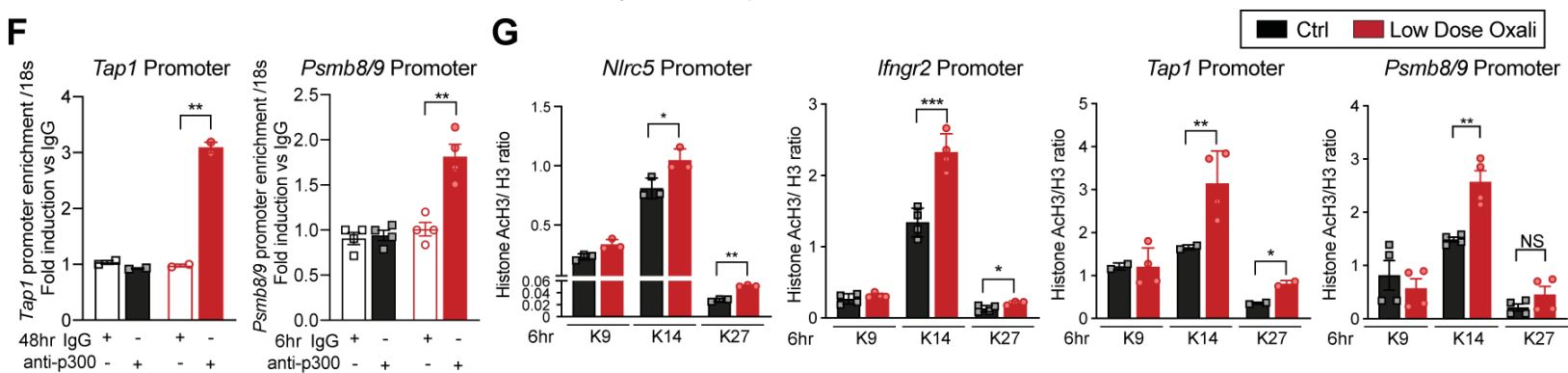
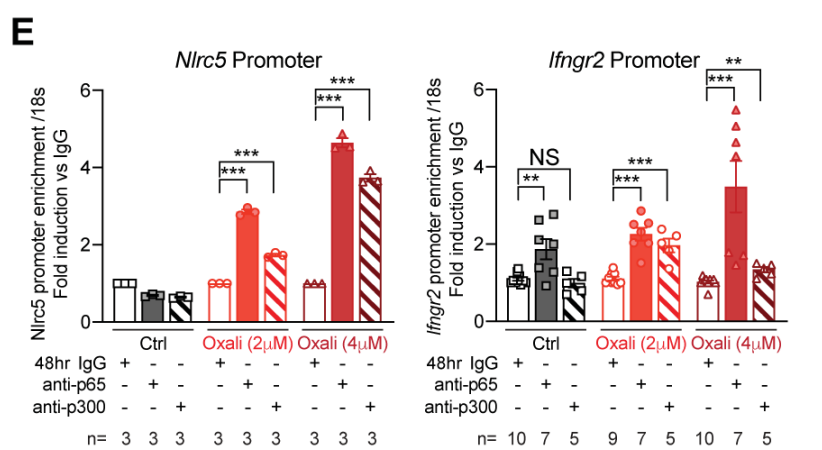
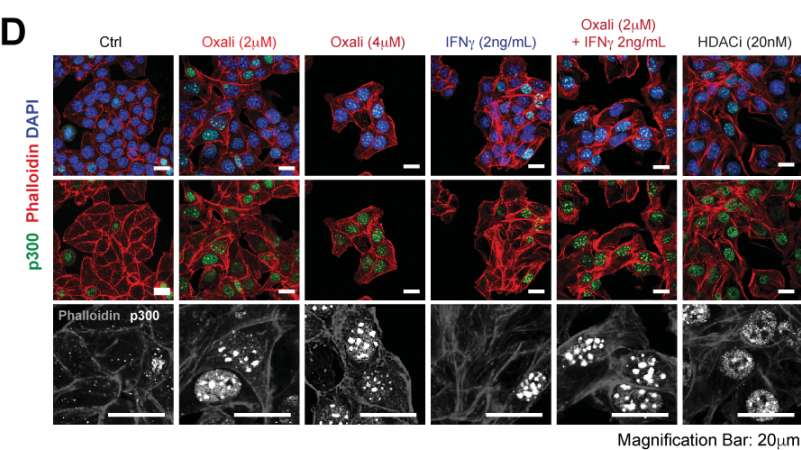
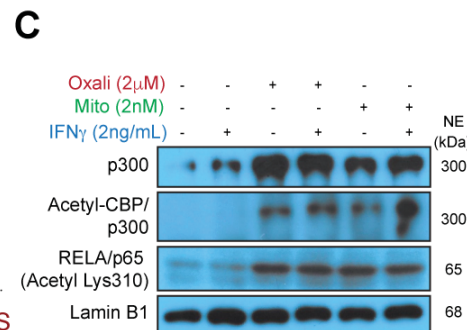
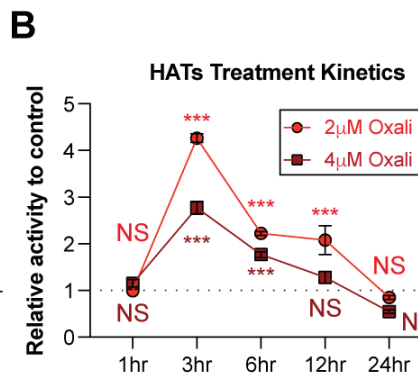
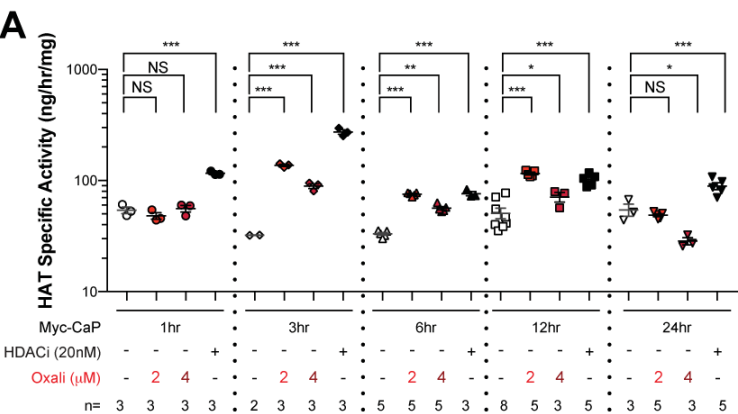


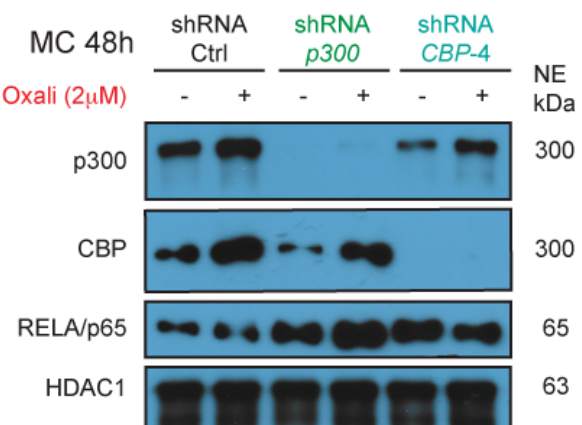
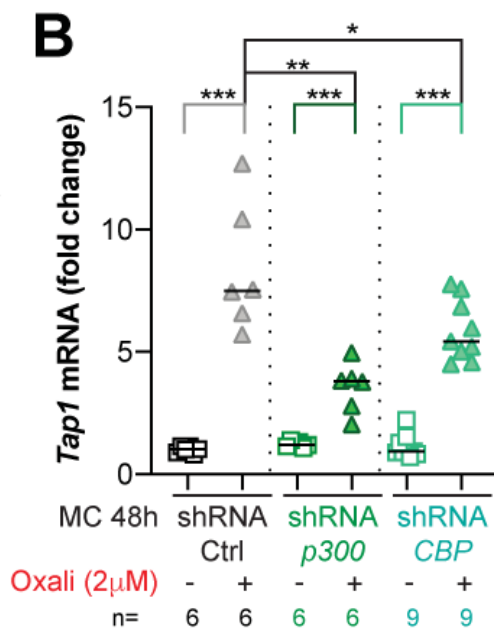
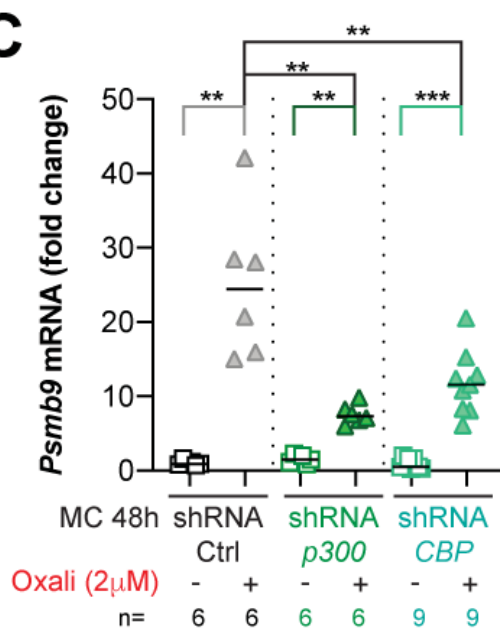
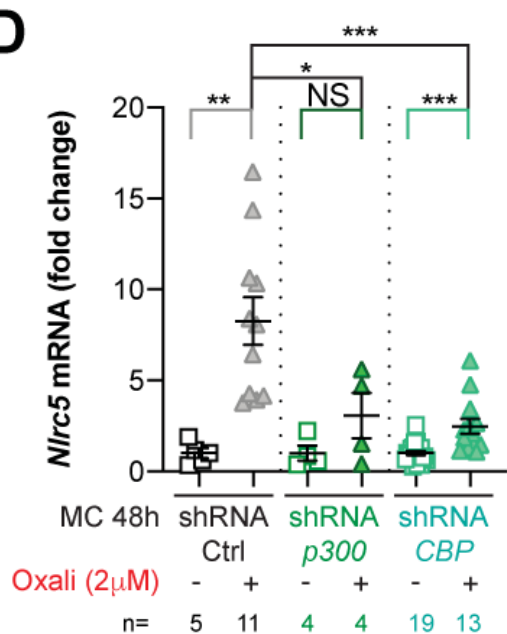
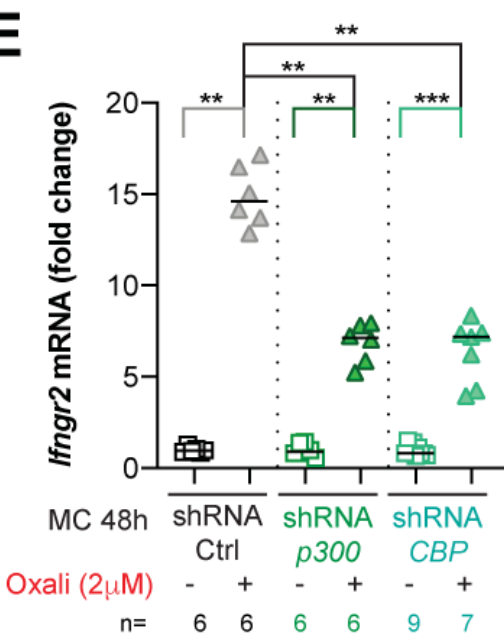
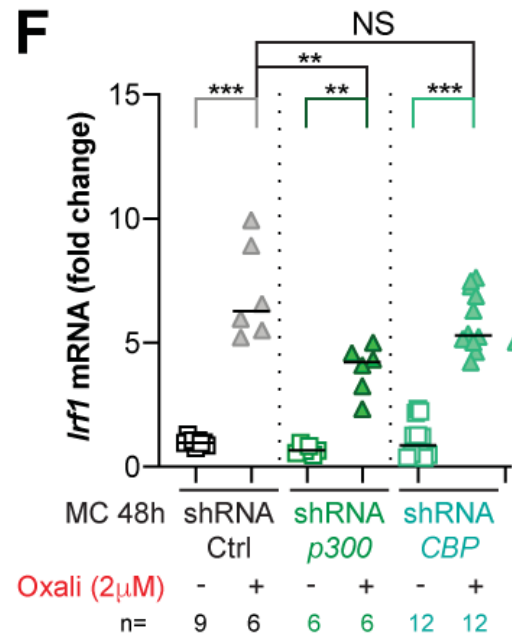
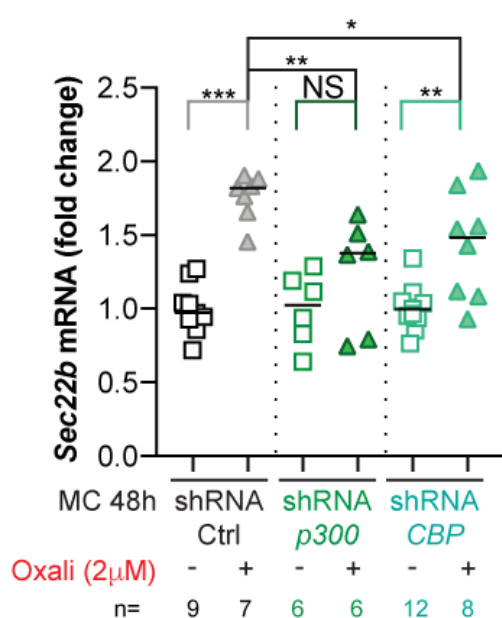
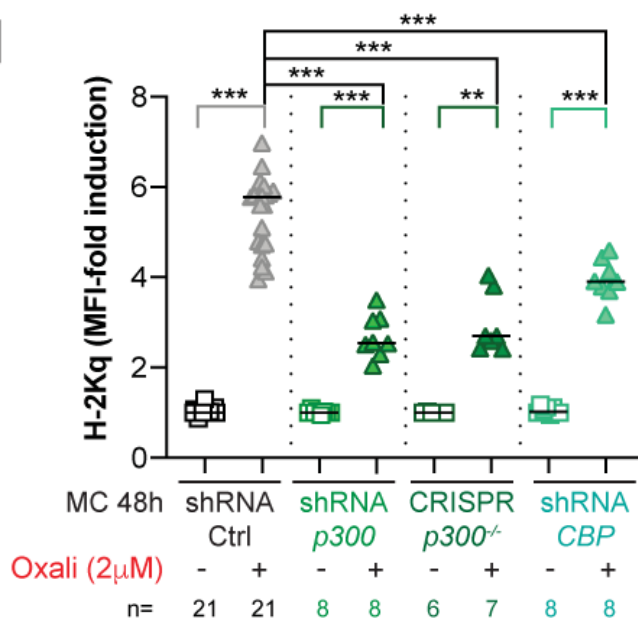
**A****B****C**

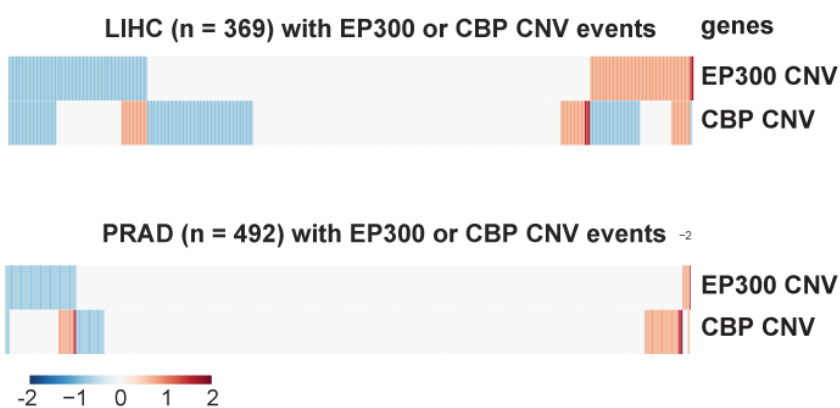
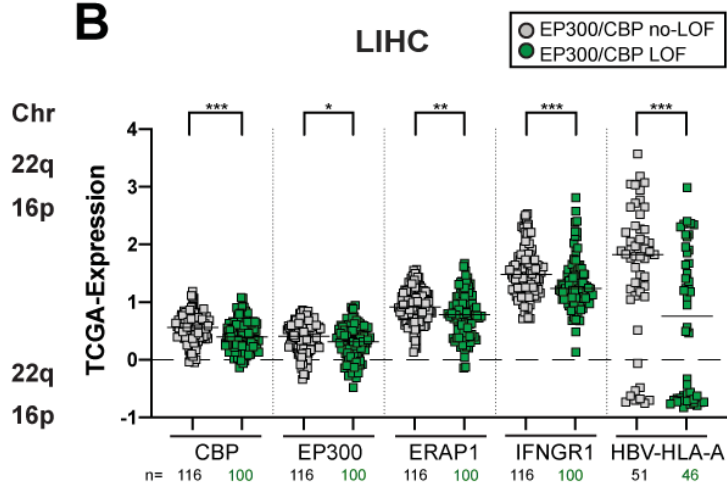
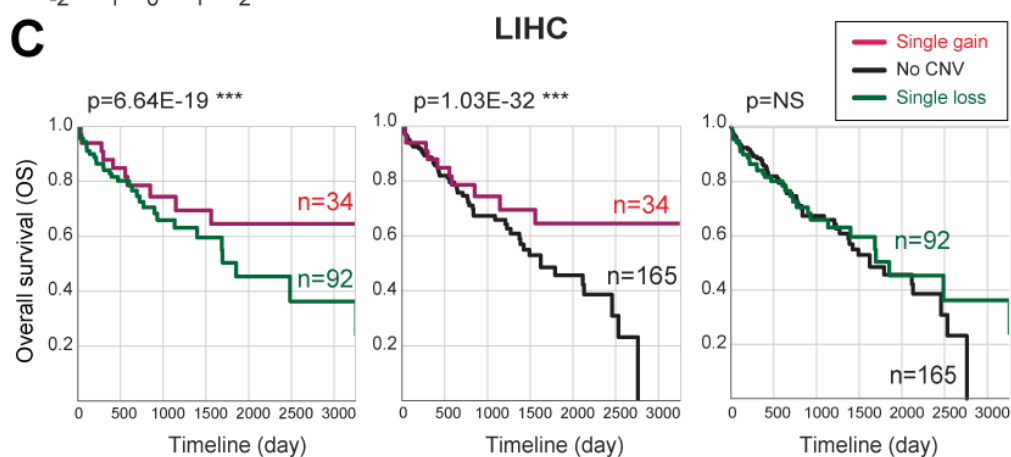
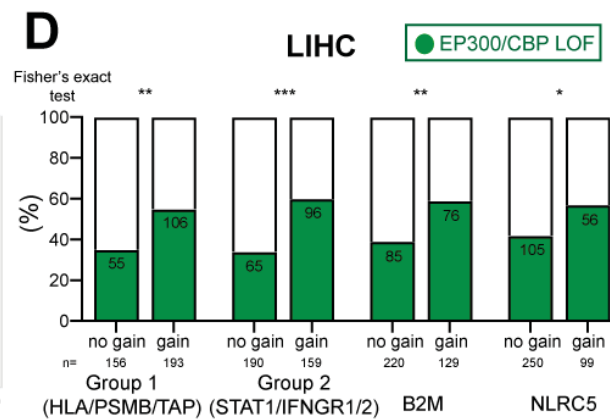
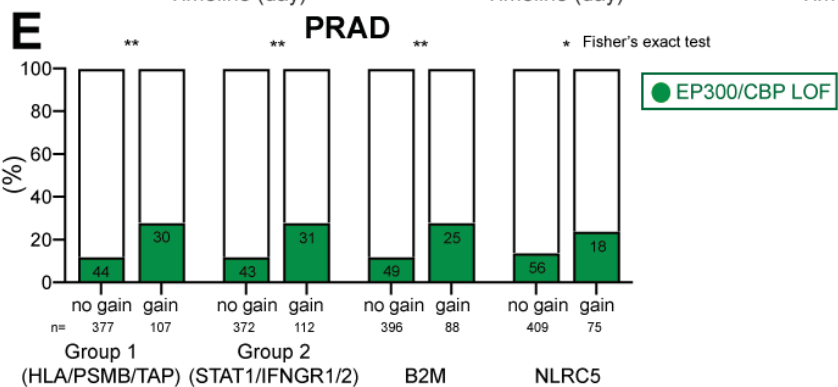




IRF1, IRF3, IRF7, IRF9, NFKB, JUNB, STAT1, STAT2, STAT3, STAT5



**A****B****C****D****E****F****G****H**

**A****Patients (TCGA)****B****C****D****E****F**